Dark matter halo properties of GAMA galaxy groups from 100 square degrees of KiDS weak lensing data

M. Viola,[1]★ M. Cacciato,[1] M. Brouwer,[1] K. Kuijken,[1] H. Hoekstra,[1] P. Norberg,[2]
A. S. G. Robotham,[3] E. van Uitert,[4,5] M. Alpaslan,[6] I. K. Baldry,[7] A. Choi,[8]
J. T. A. de Jong,[1] S. P. Driver,[3,9] T. Erben,[5] A. Grado,[10] Alister W. Graham,[11]
C. Heymans,[8] H. Hildebrandt,[5] A. M. Hopkins,[12] N. Irisarri,[1] B. Joachimi,[4]
J. Loveday,[13] L. Miller,[14] R. Nakajima,[5] P. Schneider,[5] C. Sifón[1]
and G. Verdoes Kleijn[15]

[1]*Leiden Observatory, Leiden University, Niels Bohrweg 2, NL-2333 CA Leiden, the Netherlands*
[2]*ICC, Department of Physics, Durham University, South Road, Durham DH1 3LE, UK*
[3]*ICRAR, School of Physics, University of Western Australia, 35 Stirling Highway, Crawley, WA 6009, Australia*
[4]*Department of Physics and Astronomy, University College London, Gower Street, London WC1E 6BT, UK*
[5]*Argelander-Institut für Astronomie, Auf dem Hügel 71, D-53121 Bonn, Germany*
[6]*NASA Ames Research Centre, N232, Moffett Field, Mountain View, CA 94035, USA*
[7]*Astrophysics Research Institute, Liverpool John Moores University, IC2, Liverpool Science Park, 146 Brownlow Hill, Liverpool L3 5RF, UK*
[8]*Scottish Universities Physics Alliance, Institute for Astronomy, University of Edinburgh, Royal Observatory, Blackford Hill, Edinburgh EH9 3HJ, UK*
[9]*Scottish Universities' Physics Alliance (SUPA), School of Physics and Astronomy, University of St Andrews, North Haugh, St Andrews, KY16 9SS, UK*
[10]*INAF-Osservatorio Astronomico di Capodimonte, Via Moiariello 16, I-80131 Napoli, Italy*
[11]*Centre for Astrophysics and Supercomputing, Swinburne University of Technology, Hawthorn, VIC 3122, Australia*
[12]*Australian Astronomical Observatory, PO Box 915, North Ryde, NSW 1670, Australia*
[13]*Astronomy Centre, University of Sussex, Falmer, Brighton BN1 9QH, UK*
[14]*Department of Physics, Oxford University, Keble Road, Oxford OX1 3RH, UK*
[15]*Kapteyn Astronomical Institute, University of Groningen, PO Box 800, NL-9700 AV Groningen, the Netherlands*

ABSTRACT

The Kilo-Degree Survey is an optical wide-field survey designed to map the matter distribution in the Universe using weak gravitational lensing. In this paper, we use these data to measure the density profiles and masses of a sample of ∼1400 spectroscopically identified galaxy groups and clusters from the Galaxy And Mass Assembly survey. We detect a highly significant signal (signal-to-noise-ratio ∼120), allowing us to study the properties of dark matter haloes over one and a half order of magnitude in mass, from $M \sim 10^{13}$–$10^{14.5} \, h^{-1} \, M_\odot$. We interpret the results for various subsamples of groups using a halo model framework which accounts for the mis-centring of the brightest cluster galaxy (used as the tracer of the group centre) with respect to the centre of the group's dark matter halo. We find that the density profiles of the haloes are well described by an NFW profile with concentrations that agree with predictions from numerical simulations. In addition, we constrain scaling relations between the mass and a number of observable group properties. We find that the mass scales with the total r-band luminosity as a power law with slope $1.16 \pm 0.13 \, (1\sigma)$ and with the group velocity dispersion as a power law with slope $1.89 \pm 0.27 \, (1\sigma)$. Finally, we demonstrate the potential of weak lensing studies of groups to discriminate between models of baryonic feedback at group scales by comparing our results with the predictions from the Cosmo-OverWhelmingly Large Simulations project, ruling out models without AGN feedback.

Key words: methods: observational – methods: statistical – galaxies: groups: general – galaxies: haloes – dark matter – large-scale structure of Universe.

1 INTRODUCTION

Galaxy groups are the most common structures in the Universe, thus representing the typical environment in which galaxies are found.

*E-mail: viola@strw.leidenuniv.nl

In fact, most galaxies are either part of a group or have been part of a group at a certain point in time (Eke et al. 2004). However, group properties are not as well studied compared to those of more massive clusters of galaxies, or individual galaxies. This is because groups are difficult to identify due to the small number of (bright) members. Identifying groups requires a sufficiently deep[1] spectroscopic survey with good spatial coverage, that is near 100 per cent complete. Even if a sample of groups is constructed, the typically small number of members per group prevents reliable direct dynamical mass estimates (Carlberg et al. 2001; Robotham et al. 2011). It is possible to derive ensemble averaged properties (e.g. More, van den Bosch & Cacciato 2009b), but the interpretation ultimately relies on either a careful comparison to numerical simulations or an assumption of an underlying analytical model (e.g. More et al. 2011).

For clusters of galaxies, the temperature and luminosity of the hot X-ray emitting intracluster medium can be used to estimate masses under the assumption of hydrostatic equilibrium. Simulations (e.g. Rasia et al. 2006; Nagai, Vikhlinin & Kravtsov 2007) and observations (e.g. Mahdavi et al. 2013) indicate that the hydrostatic masses are biased somewhat low, due to bulk motions and non-thermal pressure support, but correlate well with the mass. In principle, it is possible to apply this technique to galaxy groups; however, this is observationally expensive given their faintness in X-rays, and consequently samples are generally small (e.g. Sun et al. 2009; Eckmiller, Hudson & Reiprich 2011; Kettula et al. 2013; Finoguenov et al. 2015; Pearson et al. 2015) and typically limited to the more massive systems.

Furthermore, given their lower masses and the corresponding lower gravitational binding energy, baryonic processes, such as feedback from star formation and active galactic nuclei (AGN) are expected to affect groups more than clusters (e.g. McCarthy et al. 2010; Le Brun et al. 2014). This may lead to increased biases in the hydrostatic mass estimates. The mass distribution in galaxy groups is also important for predictions of the observed matter power spectrum, and recent studies have highlighted that baryonic processes can lead to significant biases in cosmological parameter constraints from cosmic shear studies if left unaccounted for (e.g. Semboloni et al. 2011; van Daalen et al. 2011; Semboloni, Hoekstra & Schaye 2013).

The group environment also plays an important role in determining the observed properties of galaxies. For example, there is increasing evidence that star formation quenching happens in galaxy groups (Robotham et al. 2013; Wetzel et al. 2014), due to ram pressure stripping, mergers, or AGN jets in the centre of the halo (Dubois et al. 2013). The properties of galaxies and groups of galaxies correlate with properties of their host dark matter halo (Vale & Ostriker 2004; Behroozi, Conroy & Wechsler 2010; Moster et al. 2010; Moster, Naab & White 2013), and the details of those correlations depend on the baryonic processes taking place inside the haloes (Le Brun et al. 2014). Hence, characterization of these correlations is crucial to understand the effects of environment on galaxy evolution.

The study of galaxy groups is thus of great interest, but constraining models of galaxy evolution using galaxy groups requires both reliable and complete group catalogues over a relatively large part of the sky and unbiased measurements of their dark matter halo properties. In the past decade, several large galaxy surveys have

become available, and significant effort has been made to reliably identify bound structures and study their properties (Eke et al. 2004; Gerke et al. 2005; Berlind et al. 2006; Brough et al. 2006; Knobel et al. 2009). In this paper, we use the group catalogue presented in Robotham et al. (2011) (hereafter R+11) based on the three equatorial fields of the spectroscopic Galaxy And Mass Assembly survey (hereafter GAMA; Driver et al. 2011). For the reasons outlined above, determining group masses using 'traditional' techniques is difficult. Fortunately, weak gravitational lensing provides a direct way to probe the mass distribution of galaxy groups (e.g. Hoekstra et al. 2001; Parker et al. 2005; Leauthaud et al. 2010). It uses the tiny coherent distortions in the shapes of background galaxies caused by the deflection of light rays from foreground objects, in our case galaxy groups (e.g. Bartelmann & Schneider 2001). Those distortions are directly proportional to the tidal field of the gravitational potential of the foreground lenses, hence allowing us to infer the properties of their dark matter haloes without assumptions about their dynamical status. The typical distortion in the shape of a background object caused by foreground galaxies is much smaller than its intrinsic ellipticity, preventing a precise mass determination for individual groups. Instead, we can only infer the ensemble averaged properties by averaging the shapes of many background galaxies around many foreground lenses, under the assumption that galaxies are randomly oriented in the Universe.

The measurement of the lensing signal involves accurate shape estimates, which in turn require deep, high-quality imaging data. The shape measurements presented in this paper are obtained from the ongoing Kilo-Degree Survey (KiDS; de Jong et al. 2015). KiDS is an optical imaging survey with the OmegaCAM wide-field imager (Kuijken 2011) on the VLT survey telescope (Capaccioli & Schipani 2011; de Jong et al. 2013) that will eventually cover 1500 deg^2 of the sky in four bands (*ugri*). Crucially, the survey region of GAMA fully overlaps with KiDS. The depth of the KiDS data and its exquisite image quality are ideal to use weak gravitational lensing as a technique to measure halo properties of the GAMA groups, such as their masses. This is the main focus of this paper, one of a set of articles about the gravitational lensing analysis of the first and second KiDS data releases (de Jong et al. 2015). Companion papers will present a detailed analysis of the properties of galaxies as a function of environment (van Uitert et al., in preparation), the properties of satellite galaxies in groups (Sifón et al. 2015), as well as a technical description of the lensing and photometric redshift measurements (Kuijken et al. 2015, K+15 hereafter).

In the last decade, weak gravitational lensing analyses of large optical surveys have become a standard tool to measure average properties of dark matter haloes (Brainerd, Blandford & Smail 1996; Fischer et al. 2000; Hoekstra 2004; Sheldon et al. 2004, 2009; Parker et al. 2005; Heymans et al. 2006; Mandelbaum et al. 2006; Johnston et al. 2007; van Uitert et al. 2011; Choi et al. 2012; Leauthaud et al. 2012a; Velander et al. 2014; Coupon et al. 2015; Hudson et al. 2015). However, the interpretation of the stacked lensing signal of haloes with different properties is not trivial. Haloes with different masses are stacked together, and a simple fit of the signal using some function describing an average halo profile, like a Navarro-Frenk-White profile (Navarro, Frenk & White 1995, hereafter NFW), can provide biased measurements. A natural framework to describe the statistical weak lensing signal is the so-called halo model (Cooray & Sheth 2002; van den Bosch et al. 2013). It provides a statistical description of the way observable galaxy properties correlate with the mass of dark matter haloes taking into account the halo mass function, the halo abundance and their large scale bias.

---

[1] Fainter than the characteristic galaxy luminosity L^* where the power-law form of the luminosity function cuts off.

The outline of this paper is as follows. In Section 2, we summarize the basics of weak lensing theory. We describe the data used in this work in Section 3, and we summarize the halo model framework in Section 4. In Section 5, we present our lensing measurements of the GAMA galaxy groups, and in Section 6, we derive scaling relations between lensing masses and optical properties of the groups. We conclude in Section 7.

The relevant cosmological parameters entering in the calculation of distances and in the halo model are taken from the Planck best-fitting cosmology (Planck Collaboration XVI et al. 2014): $\Omega_m = 0.315$, $\Omega_\Lambda = 0.685$, $\sigma_8 = 0.829$, $n_s = 0.9603$ and $\Omega_b h^2 = 0.022\,05$. Throughout the paper, we use M_{200} as a measure for the masses of the groups as defined by 200 times the mean density (and corresponding radius, noted as R_{200}).

2 STATISTICAL WEAK GRAVITATIONAL LENSING

Gravitational lensing refers to the deflection of light rays from distant objects due to the presence of matter along the line of sight. Overdense regions imprint coherent tangential distortions (shear) in the shape of background objects (hereafter sources). Galaxies form and reside in dark matter haloes, and as such, they are biased tracers of overdense regions in the Universe. For this reason, one expects to find non-vanishing shear profiles around galaxies, with the strength of this signal being stronger for groups of galaxies as they inhabit more massive haloes. This effect is stronger in the proximity of the centre of the overdensity and becomes weaker at larger distances.

Unfortunately, the coherent distortion induced by the host halo of a single galaxy (or group of galaxies) is too weak to be detected. We therefore rely on a statistical approach in which many galaxies or groups that share similar observational properties are stacked together. Average halo properties (e.g. masses, density profiles) are then inferred from the resulting high signal-to-noise shear measurements. This technique is commonly referred to as 'galaxy–galaxy lensing', and it has become a standard approach for measuring masses of galaxies in a statistical sense.

Given its statistical nature, galaxy–galaxy lensing can be viewed as a measurement of the cross-correlation of some baryonic tracer δ_g and the matter density field δ_m:

$$\xi_{gm}(\boldsymbol{r}) = \langle \delta_g(\boldsymbol{x}) \delta_m(\boldsymbol{x} + \boldsymbol{r}) \rangle_x \,, \tag{1}$$

where $\boldsymbol{r}$ is the three-dimensional comoving separation. The equation above can be related to the projected matter surface density around galaxies via the Abel integral:

$$\Sigma(R) = \bar{\rho}_m \int_0^{\pi_s} [1 + \xi_{gm}(\sqrt{R^2 + \Pi^2})]\, d\Pi \,, \tag{2}$$

where R is the comoving projected separation from the galaxy, π_s the position of the source galaxy, $\bar{\rho}_m$ is the mean density of the Universe and Π is the line-of-sight separation.[2] Being sensitive to the density *contrast*, the shear is actually a measure of the excess surface density (ESD hereafter):

$$\Delta\Sigma(R) = \bar{\Sigma}(\leq R) - \Sigma(R) \,, \tag{3}$$

where $\bar{\Sigma}(\leq R)$ just follows from $\Sigma(R)$ via

$$\bar{\Sigma}(\leq R) = \frac{2}{R^2} \int_0^R \Sigma(R')\, R'\, dR' \,. \tag{4}$$

The ESD can finally be related to the tangential shear distortion γ_t of background objects, which is the main lensing observable:

$$\Delta\Sigma(R) = \gamma_t(R)\Sigma_{cr} \,, \tag{5}$$

where

$$\Sigma_{cr} = \frac{c^2}{4\pi G} \frac{D(z_s)}{D(z_l)D(z_l, z_s)} \,, \tag{6}$$

is a geometrical factor accounting for the lensing efficiency. In the previous equation, $D(z_l)$ is the angular diameter distance to the lens, $D(z_l, z_s)$ the angular diameter distance between the lens and the source and $D(z_s)$ the angular diameter distance to the source.

In the limit of a single galaxy embedded in a halo of mass M, one can see that equation (1) further simplifies because $\xi_{gm}(\boldsymbol{r})$ becomes the normalized matter overdensity profile around the centre of the galaxy. The stacking procedure builds upon this limiting case by performing a weighted average of such profiles accounting for the contribution from different haloes. This is best formulated in the context of the halo model of structure formation (see e.g. Cooray & Sheth 2002; van den Bosch et al. 2013), and for this reason, we will embed the whole analysis in this framework (see Section 4). In Section 3.3, we describe how the ESD profile is measured.

3 DATA

The data used in this paper are obtained from two surveys: the KiDS and the GAMA. KiDS is an ongoing ESO optical imaging survey with the OmegaCAM wide-field imager on the VLT survey telescope (de Jong et al. 2013). When completed, it will cover two patches of the sky in four bands (u, g, r, i), one in the Northern Galactic Cap and one in the south, adding up to a total area of 1500 deg^2 overlapping with the 2 degree Field Galaxy Redshift survey (2dFGRS hereafter; Colless et al. 2001). With rest-frame magnitude limits (5σ in a 2 arcsec aperture) of 24.3, 25.1, 24.9, and 23.8 in the u, g, r, and i bands, respectively, and better than 0.8 arcsec seeing in the r band, KiDS was designed to create a combined data set that included good weak lensing shape measurements and good photometric redshifts. This enables a wide range of science including cosmic shear 'tomography', galaxy–galaxy lensing and other weak lensing studies.

In this paper, we present initial weak lensing results based on observations of 100 KiDS tiles, which have been covered in all four optical bands and released to ESO as part of the first and second 'KiDS-DR1/2' data releases to the ESO community, as described in de Jong et al. (2015). The effective area after removing masks and overlaps between tiles is 68.5 deg^2.[3]

In the equatorial region, the KiDS footprint overlaps with the footprint of the GAMA spectroscopic survey (Liske et al. 2005; Baldry et al. 2010; Robotham et al. 2010; Driver et al. 2011), carried out using the AAOmega multi-object spectrograph on the Anglo-Australian Telescope. The GAMA survey is highly complete down to petrosian r-band magnitude 19.8,[4] and it covers ~180 deg^2 in

---

[2] Here and throughout the paper we assume spherical symmetry. This assumption is justified in the context of this work since we measure the lensing signal from a stack of many different haloes with different shapes, which washes out any potential halo triaxiality.

[3] A further 48 tiles from the KiDS-DR1/2, mostly in KiDS-South, were not used in this analysis since they do not overlap with GAMA.

[4] The petrosian apparent magnitudes are measured from SDSS-DR7 and they include extinction corrections (Schlegel maps).
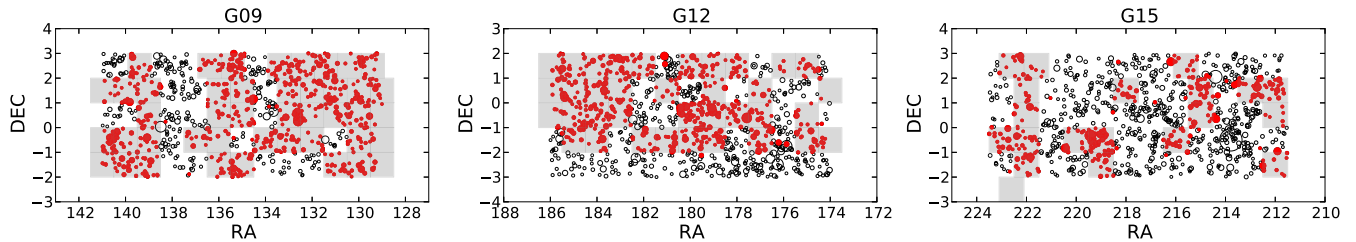
Figure 1. KiDS-ESO-DR1/2 coverage of the three equatorial GAMA fields (G09, G12, G15). Each grey box corresponds to a single KiDS tile of 1 deg². The black circles represent groups with $N_{fof} \geq 5$ in the G³Cv7 catalogue (R+11). The size of the dots is proportional to the group apparent richness. The filled red circles indicate the groups used in this analysis. These are all groups either inside a KiDS field or whose centre is separated less than 2 h^{-1} Mpc from the centre of the closest KiDS field.

Table 1. Summary of the area overlap of KiDS-DR1/2 in the three GAMA fields and the number of groups with at least five members used in this analysis. In parenthesis we quote the effective area, accounting for masks, used in this work.

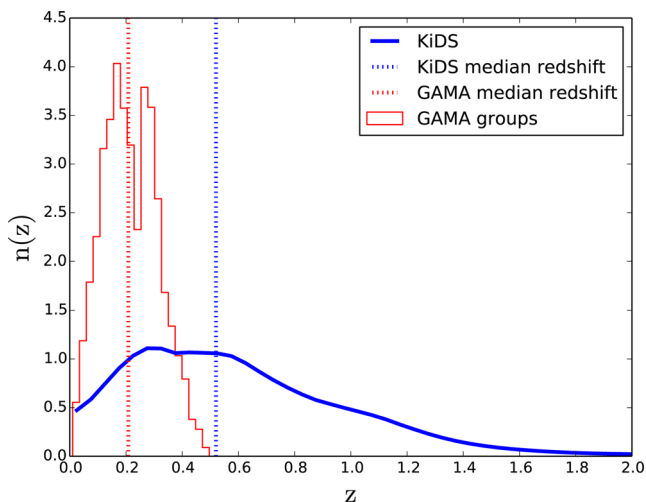| GAMA field	KiDS-DR1/2 overlap (deg²)	Number of groups
G09	44.0 (28.5)	596
G12	36.0 (25.0)	509
G15	20.0 (15.0)	308

Figure 2. Redshift distribution of the GAMA groups used in this analysis (red histogram) and the KiDS galaxies (blue lines). In the case of the GAMA groups, we use the spectroscopic redshift of the groups with at least five members (R+11), while for the KiDS galaxies the redshift distribution is computed as a weighted sum of the posterior photometric redshift distribution as provided by BPZ (Benítez 2000). The weight comes from *lens*fit, used to measure the shape of the objects (Miller et al. 2007). The two vertical lines show the median of the redshift distribution of the GAMA groups and of the KiDS sources. The two peaks in the redshift distribution of the GAMA groups are physical (and not caused by incompleteness), due to the clustering of galaxies in the GAMA equatorial fields.

the equatorial region, which allows for the identification of a large number of galaxy groups.

Fig. 1 shows the KiDS-DR1/2 coverage of the G09, G12, and G15 GAMA fields. We also show the spatial distribution of the galaxy groups in the three GAMA fields (open black circles) and the selection of groups entering in this analysis (red filled circles).

Table 1 lists the overlap between KiDS-DR1/2 and GAMA and the total number of groups used in this analysis. Fig. 2 shows the redshift distribution of the GAMA groups used in this work

and of the KiDS source galaxies, computed as a weighted sum of the posterior photometric redshift distribution as provided by BPZ (Benítez 2000). The weight comes from the *lens*fit code, which is used to measure the shape of the objects (Miller et al. 2007, see Section 3.2.1). The median redshift of the GAMA groups is $z = 0.2$, while the weighted median redshift of KiDS is 0.53. The multiple peaks in the redshift distribution of the KiDS sources result from degeneracies in the photometric redshift solution. This is discussed further in K+15. The different redshift distributions of the two surveys are ideal for a weak lensing study of the GAMA groups using the KiDS galaxies as background sources.

3.1 Lenses: GAMA Groups

One of the main products of the GAMA survey is a group catalogue, G³C (R+11), of which we use the internal version 7. It consists of 23 838 galaxy groups identified in the GAMA equatorial regions (G09, G12, G15), with over 70 000 group members. It has been constructed employing spatial and spectroscopic redshift information (Baldry et al. 2014) of all the galaxies targeted by GAMA in the three equatorial regions. The groups are found using a friends-of-friends algorithm, which links galaxies based on their projected and line-of-sight proximity. The choice of the linking length has been optimally calibrated using mock data (R+11; Merson et al. 2013) based on the Millennium simulation[5] (Springel et al. 2005b) and a semi-analytical galaxy formation model (Bower et al. 2006). Running the final group selection algorithm on the mock catalogues shows that groups with at least five GAMA galaxies are less affected by interlopers and have sufficient members for a velocity dispersion estimate (R+11). For this reason we use only such groups in our analysis. This choice leaves us with 1413 groups, in KiDS-DR1/2, 11 per cent of the full GAMA group catalogue.

Fig. 3 shows the distribution of the total group r-band luminosity as a function of the redshift of the group, the group apparent richness, which is the number of members brighter that $r = 19.8$, and the group velocity dispersion corrected for velocity uncertainty, for this subsample. These group r-band luminosity values are calculated by summing the r-band luminosity of all galaxies belonging to a group and targeted by GAMA and they also include an estimate of the contribution from faint galaxies below the GAMA flux limit, as discussed in R+11. This correction is typically very small, a few per cent at low redshift and a factor of a few at $z \sim 0.5$ since most of the luminosity comes from galaxies around $M^\star - 5 \log h \sim -20.44$ (Loveday et al. 2012, 2015), and most of the

---

[5] $(\Omega_m, \Omega_b, \Omega_\Lambda, h, \sigma_8, n_s) = (0.25, 0.045, 0.75, 0.73, 0.9, 1.0)$
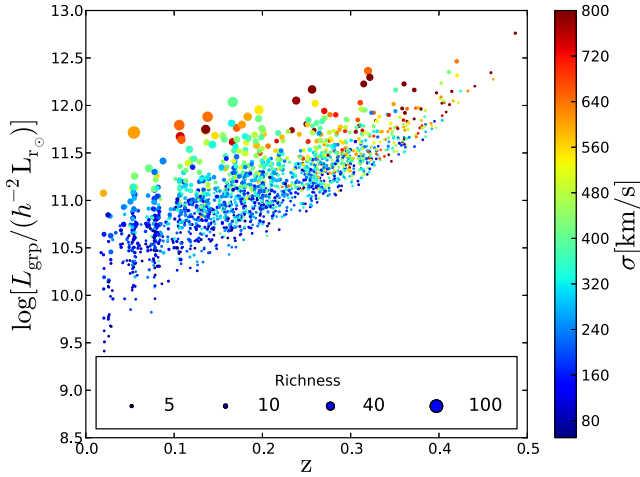
Figure 3. Total group *r*-band luminosity as a function of the redshift of the group. The size of the points is proportional to the group apparent richness and the colour of the points indicates the group velocity dispersion corrected for velocity uncertainty. The shape of the distribution is typical of a flux limited survey.

groups are sampled well below $M^\star$. Note that all absolute magnitudes and luminosities used in the paper are *k*-corrected and evolution corrected at redshift $z = 0$ (R+11). The global *k*-correction used by R+11 is compatible with the median *k*-correction of the full GAMA (McNaught-Roberts et al. 2014, fig.1 in the paper).

All the stellar masses used in this work are taken from Taylor et al. (2011), who fitted Bruzual & Charlot (2003) synthetic stellar spectra to the broad-band Sloan Digital Sky Survey (SDSS) photometry assuming a Chabrier (2003) IMF and a Calzetti et al. (2000) dust law.

3.2 Sources: KiDS galaxies

We measure the gravitational lensing effect induced by the GAMA groups using galaxy images from KiDS. We refer to K+15 for a detailed description of the pipelines used to measure shapes and photometric redshifts for those objects. We briefly summarize here the aspects of the data processing most relevant for this analysis.

3.2.1 Shape measurements

All of our lensing measurements are derived from the *r*-band exposures in KiDS. This is the band with the highest image quality of the survey, as the queue-scheduling at the telescope ensures that observations in this filter are taken in the best seeing conditions. The images are processed with the THELI pipeline, which has been optimized for lensing applications (Erben et al. 2013), and ellipticities for the galaxies are derived using the *lens*fit code (Miller et al. 2007, 2013; Kitching et al. 2008). *lens*fit takes full account of the point spread function (PSF) in the individual (dithered) exposures and prior knowledge of the ellipticity and size distributions of faint galaxies, returning an ellipticity estimate for each galaxy as well as an inverse variance weight that is related to the uncertainty of the measurement.

The average number density of galaxies with *lens*fit weight w larger than 0, and satisfying the photometric redshift cuts described in the next section, is 8.88 arcmin^{-2}, corresponding to an effective number density:

$$n_{\rm eff} = \frac{\sigma_{\epsilon^s}^2}{A} \sum_i w_i \tag{7}$$

of 4.48 galaxies per square arcmin, where A is the survey area and $\sigma_{\epsilon^s}^2 = 0.065$ is the intrinsic ellipticity variance. This is a measurement of the statistical power of the weak lensing data (see Chang et al. 2013 and K+15 for more details).

It is well known that shape measurements for galaxies with low signal-to-noise ratio and small sizes tend to be biased (e.g. Melchior & Viola 2012; Refregier et al. 2012; Miller et al. 2013; Viola, Kitching & Joachimi 2014). This 'noise-bias' stems from the non-linear transformations of the image pixels involved in the derivation of galaxy image shapes. It has the form of a multiplicative bias, and a calibration of the shape measurements is typically required in order to get an unbiased shear estimator. In this paper, we use the same calibration that was determined in Miller et al. (2013). This calibration depends on the signal-to-noise and the size of the objects and needs to be applied, in an average sense, to the recovered shear field. In addition to this multiplicative bias, shape measurements can also be affected by an additive bias caused by a non-perfect PSF deconvolution, centroid bias and pixel level detector effects. This bias can be empirically quantified and corrected for directly from the data, using the residual average ellipticity over the survey area. More detail on these ~10 per cent bias corrections can be found in K+15.

The analysis presented in this paper has been applied to four different ellipticity catalogues. Three of these catalogues were generated by rescaling all the ellipticity measurements by some factors unknown to the team and chosen by a colleague, Matthias Bartelmann,[6] external to the collaboration. The amplitude of the rescaling has been chosen such that the cosmological parameters derived from a cosmic shear analysis using the four blind catalogues would not differ more than 10σ, where sigma is the error from the Planck cosmological papers. We refer to this procedure as *blinding*, and we have used it to mitigate confirmation bias in our data analysis. The authors asked our external to *unblind* the true shear catalogues only just before paper submission. The authors were not allowed to change any of the results after the unblinding, without documenting those changes. Whilst the shear was blind, we did not blind measurements of group properties, such as their luminosity, or measurements of the source photometric redshifts.

3.2.2 Photometric redshift measurements

The observable lensing distortion depends on the distances to the lens and source (equation 6). Redshifts to the lenses are known from the GAMA spectroscopy, but for the sources we need to resort to photometric redshifts derived from the KiDS-ESO-DR1/2 ugri images in the ESO data release. Processing and calibration of these images is done using the Astro-WISE environment (McFarland et al. 2013), and flux and colour measurements use the 'Gaussian Aperture and Photometry' technique designed to correct aperture photometry for seeing differences (Kuijken 2008). These colours form the basis of the photometric redshift estimates, obtained with BPZ (Benítez 2000; Hildebrandt et al. 2012). After extensive tests, we reject galaxies whose photometric redshift posterior distribution

---

[6] bartelmann@uni-heidelberg.de

$p(z)$ peaks outside the range [0.005,1.2] (K+15). In what follows the $p(z)$ for each source is used in the calculation of distances, and in particular in the calculation of the critical surface density (see equation 6). K+15 show that if the peak of each source's $p(z)$ had been used as the estimate of the redshift, the average value of Σ_{cr} and hence the average ESD would have been underestimated by ~ 10 per cent .

3.3 Measurement of the stacked ESD profile

The shape measurement algorithm used in this work, *lens*fit, provides measurements of the galaxy ellipticities (ϵ_1, ϵ_2) with respect to an equatorial coordinate system.

For each source–lens pair, we compute the tangential ϵ_t and cross component ϵ_x of the source's ellipticity around the position of the lens,

$$\begin{pmatrix} \epsilon_t \\ \epsilon_x \end{pmatrix} = \begin{pmatrix} -\cos(2\phi) & -\sin(2\phi) \\ \sin(2\phi) & -\cos(2\phi) \end{pmatrix} \begin{pmatrix} \epsilon_1 \\ \epsilon_2 \end{pmatrix}, \quad (8)$$

where ϕ is the position angle of the source with respect to the lens. The average of the tangential ellipticity of a large number of galaxies in the same area of the sky is an unbiased estimate of the shear. On the other hand, the average of the cross ellipticity over many sources should average to zero. For this reason, the cross-ellipticity is commonly used as an estimator of possible systematics in the measurements. Each lens-source pair is then assigned a weight

$$\tilde{w}_{ls} = w_s \tilde{\Sigma}_{cr}^{-2}, \quad (9)$$

which is the product of the *lens*fit weight w_s assigned to the given source ellipticity, and a geometric term $\tilde{\Sigma}_{cr}$ which downweights lens-source pairs that are close in redshift and therefore less sensitive to lensing. We compute the 'effective critical surface density' for each pair from the spectroscopic redshift of the lens z_l and the full posterior redshift distribution of the source, $p(z_s)$:

$$\tilde{\Sigma}_{cr}^{-1} = \frac{4\pi G}{c^2} \int_{z_l}^{\infty} \frac{D_l(z_l)D_{ls}(z_l, z_s)}{D_s(z_s)} p(z_s) \, dz_s . \quad (10)$$

Finally, following equation (5), we compute the ESD in bins of projected distance R to the lenses:

$$\Delta\Sigma(R) = \left(\frac{\sum_{ls} \tilde{w}_{ls}\epsilon_t \tilde{\Sigma}_{cr}}{\sum_{ls} \tilde{w}_{ls}} \right) \frac{1}{1 + K(R)}, \quad (11)$$

where the sum is over all source–lens pairs in the distance bin, and

$$K(R) = \frac{\sum_{ls} \tilde{w}_{ls}m_s}{\sum_{ls} \tilde{w}_{ls}}, \quad (12)$$

is an average correction to the ESD profile that has to be applied to correct for the multiplicative noise bias m in the *lens*fit shear estimates. Typically, the value of the $K(R)$ correction is around 0.1, largely independent of the scale at which it is computed.

Fig. 4 shows the stacked ESD profile for all groups either inside a KiDS field or whose centre is separated by less than $2\,h^{-1}$ Mpc from the centre of the closest KiDS field. It shows a highly significant detection of the lensing signal (signal-to-noise ratio $\sim$120). We note that the signal to noise is very poor at scales smaller than $20\,h^{-1}$ kpc. This is due to the fact that many objects close to the group centres are blended, and *lens*fit assigns them a vanishing weight. We exclude those scales from any further analysis presented in this paper.

For reference, we also show the best-fitting singular isothermal sphere (SIS) and NFW models to the stacked ESD signal. In the
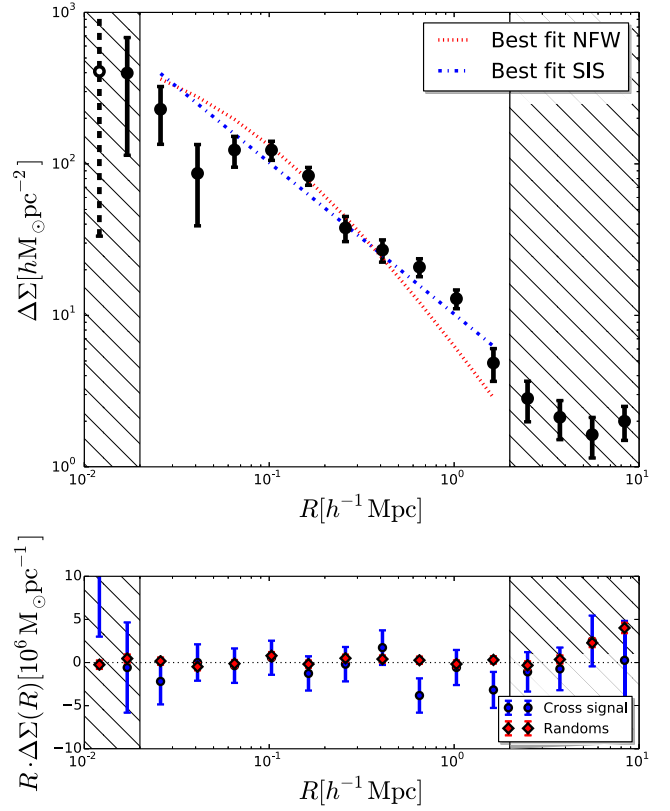

Figure 4. Top panel: ESD profile measured from a stack of all GAMA groups with at least five members (black points). Here, we choose the BCG as the group centre. The open white circle with dashed error bars indicates a negative $\Delta\Sigma$. The dotted red line and the dash–dotted blue line show the best fits to the data of NFW (Navarro et al. 1995) and SIS profiles, respectively. Neither of the single-parameter models provides a good fit to the data, highlighting that complex modelling of the signal is required. Bottom panel: ESD profile, multiplied by R to enhance features at large radii, measured from the cross-component of the ellipticities for these same groups (blue points) and measured around random points using the same redshift distribution of the groups (red points). We only use measurements at scales outside the dashed areas for the rest of the paper.

case of the NFW model, the halo concentration is fixed using the Duffy et al. (2008) mass–concentration relation. Neither of the two single-parameter models provides a good fit to the data ($\chi^2_{red} > 2.5$), highlighting how a more complex modelling of the signal is required (see Section 4).

Fig. 4 also includes two tests for residual systematic errors in the data: the cross-component of the signal and the signal measured around random points in the KiDS tiles. On scales larger than $2\,h^{-1}$ Mpc, small but significant deviations are evident. We believe that one possible origin of the non-vanishing signal around random points at these scales is due to the incomplete azimuthal average of galaxy ellipticities, but we cannot exclude some large-scale systematics in the shear data. The current patchy coverage of lensing data complicates a detailed analysis and here we simply note that the effect is small (less than 10 per cent of the signal at $2\,h^{-1}$ Mpc) and exclude data on scales larger than $2\,h^{-1}$ Mpc. Future analyses based on more uniform coverage of the GAMA area from the KiDS survey will need to address these potential issues.

To summarize, in the rest of the paper we will use only projected distances in the range $(0.02–2)\,h^{-1}$ Mpc. Both the cross-component
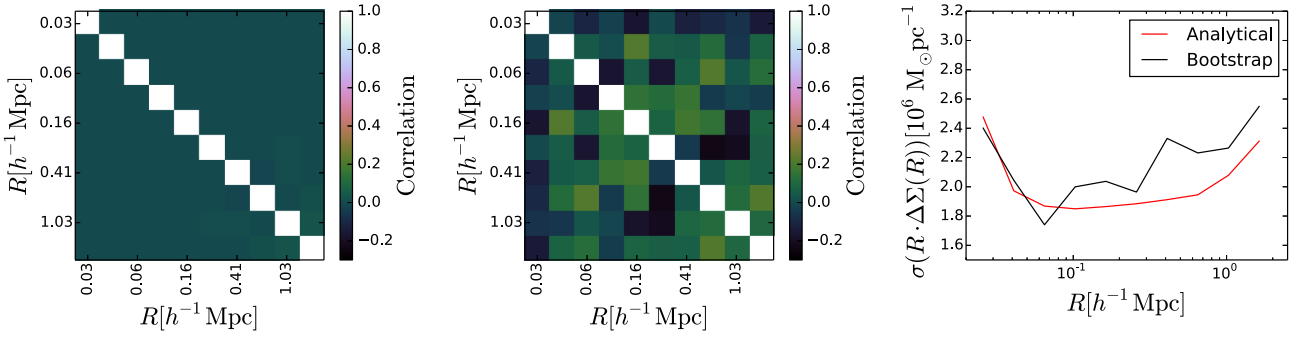
Figure 5. Left panel: ESD correlation matrix between different radial bins estimated from the data. This matrix accounts for shape noise and the effect of the mask and is computed as described in Section 3.4. Middle panel: ESD correlation matrix between different radial bins estimated using a bootstrap technique. It accounts for cosmic variance as well as shape noise. Right panel: comparison of the square root of the diagonal elements of the two covariance matrices as a function of distance from the group centre (here the BCG). Note the lower noise in the left-hand panel and the small but significant correlation between the largest-radial bins, which is a consequence of the many survey edges.

of the shear and the signal around random points are consistent with a null-detection over these scales.

3.4 Statistical error estimate

In a stacking analysis with many foreground lenses, the ellipticity of any source galaxy can contribute to the $\Delta\Sigma_i$ estimate in multiple radial bins i of different lenses. We summarize here how we compute the resulting covariances between the ESD estimates $\Delta\Sigma_i$ from the data.

We start from equation (11), which gives the expression for $\Delta\Sigma_i$. For simplicity, we drop in what follows the noise bias correction factor $1 + K(R)$ as it can be considered to have been absorbed in the effective critical density $\tilde{\Sigma}_{\rm cr}$.

We first rearrange the sum in equation (11) to separate the contributions from each source s, by summing first over all lenses l that project within the radial bin i from source s; for each source s we denote this set of lenses as i_s. We can then rewrite equation (11) as

$$\Delta\Sigma_i = \frac{\sum_s w_s \left(\epsilon_{1s} C_{si} + \epsilon_{2s} S_{si}\right)}{\sum_s w_s Z_{si}}, \tag{13}$$

where C, S, and Z are sums over the lenses

$$C_{si} = \sum_{l \in i_s} -\tilde{\Sigma}_{{\rm cr,ls}}^{-1} \cos(2\phi_{\rm ls}), \tag{14}$$

$$S_{si} = \sum_{l \in i_s} -\tilde{\Sigma}_{{\rm cr,ls}}^{-1} \sin(2\phi_{\rm ls}), \tag{15}$$

and

$$Z_{si} = \sum_{l \in i_s} \tilde{\Sigma}_{{\rm cr,ls}}^{-2}. \tag{16}$$

Since each ϵ_{ks} is an independent estimate of the shear field, where $k = 1,2$, the ESD covariance between radial bins i and j can then be easily written as

$$\mathbf{Cov}_{ij} = \frac{\sum_s \sigma_\epsilon^2 w_s^2 \left(C_{si} C_{sj} + S_{si} S_{sj}\right)}{(\sum_s w_s Z_{si})(\sum_s w_s Z_{sj})}, \tag{17}$$

where $\sigma_\epsilon^2 = 0.078$ is the ellipticity dispersion weighted with the *lens*fit weight, for one component of the ellipticity. We compute this number from the whole KiDS-ESO-DR1/2 area.

Equation (17) can be generalized to also compute the covariance between the ESD estimates for two different lens samples m and n:

$$\mathbf{Cov}_{mnij} = \frac{\sum_s \sigma_\epsilon^2 w_s^2 \left(C_{si,m} C_{sj,n} + S_{si,m} S_{sj,n}\right)}{(\sum_s w_s Z_{si,m})(\sum_s w_s Z_{sj,n})}, \tag{18}$$

by restricting the sums for the C, S, and Z terms to lenses in the relevant samples.

We test the accuracy of the above calculation, which does not account for cosmic variance, against the covariance matrix obtained via a bootstrapping technique. Specifically, we bootstrap the signal measured in each of the 1 deg^2 KiDS tiles. We limit the comparison to the case in which all groups are stacked together[7] and compute the signal in 10 logarithmically spaced radial bins between $20\,h^{-1}$ kpc and $2\,h^{-1}$ Mpc. This leads to an ESD covariance matrix with 55 independent entries, which can be constrained by the 100 KiDS tiles used in this analysis. The corresponding matrix is shown in Fig. 5 together with the correlation matrix obtained from equation (17). The small but significant correlation between the largest radial bins is a consequence of the survey edges. We further show the diagonal errors obtained with the two methods, labelled Analytical and Bootstrap. Based on the work by Norberg et al. (2009), we might expect that the bootstrapping technique leads to somewhat larger error bars, although on larger scales this trend may be counteracted to some degree by the limited independence of our bootstrap regions. However, the conclusions of Norberg et al. (2009) are based on an analysis of galaxy clustering, and a quantitative translation of their results to our galaxy–galaxy lensing measurements is not easy and beyond the scope of this work. The difference between the error estimates using these two independent methods is at most 10 per cent at scales larger than $300\,h^{-1}$ kpc. Based on the results of this test, we consider the covariance matrix estimated from equation (17) to be a fair estimation of the true covariance in the data, and we use it throughout the paper. In our likelihood analyses of various models for the data (see next section), we account for the covariance between the radial bins as well as between the different lens samples used to compute the stacked signal. We note that future analyses with greater statistical power, for example those based on the full KiDS and GAMA overlap, and studies focusing on larger scales than those considered in this analysis, will need to properly

---

[7] If the signal is split further into several bins according to some property of the group, we expect the relative contribution from cosmic variance compared to the contribution from shape noise to be even lower.

evaluate the full covariance matrix that incorporates the cosmic variance contribution that is negligible in this work.

4 HALO MODEL

In this section, we describe the halo model (e.g. Seljak 2000; Cooray & Sheth 2002), which we use to provide a physical interpretation of our data. We closely follow the methodology introduced in van den Bosch et al. (2013) and successfully applied to SDSS galaxy–galaxy lensing data in Cacciato et al. (2013).

This model provides the ideal framework to describe the statistical weak lensing signal around galaxy groups. It is based on two main assumptions:

(i) a statistical description of dark matter halo properties (i.e. their average density profile, their abundance, and their large scale bias);

(ii) a statistical description of the way galaxies with different observable properties populate dark matter haloes.

As weak gravitational lensing is sensitive to the mass distribution projected along the line of sight, the quantity of interest is the ESD profile, defined in equation (3), which is related to the galaxy–matter cross-correlation via equation (2). Under the assumption that each galaxy group resides in a dark matter halo, its average $\Delta\Sigma(R, z)$ profile can be computed using a statistical description of how galaxies are distributed over dark matter haloes of different mass and how these haloes cluster. Specifically, it is fairly straightforward to obtain the two-point correlation function, $\xi_{\mathrm{gm}}(r, z)$, by Fourier transforming the galaxy–dark matter power-spectrum, $P_{\mathrm{gm}}(k, z)$, i.e.

$$\xi_{\mathrm{gm}}(r, z) = \frac{1}{2\pi^2} \int_0^\infty P_{\mathrm{gm}}(k, z) \frac{\sin(kr)}{kr} k^2 \, \mathrm{d}k, \tag{19}$$

with k the wavenumber, and the subscript 'g' and 'm' standing for 'galaxy' and 'matter'.

In what follows, we will use the fact that, in Fourier space, the matter density profile of a halo of mass M at a redshift z can be described as $M \tilde{u}_{\mathrm{h}}(k|M, z)$, where $M \equiv 4\pi(200\bar{\rho})R_{200}^3/3$, and $\tilde{u}_{\mathrm{h}}(k|M)$ is the Fourier transform of the normalized *dark* matter density profile of a halo of mass M.[8] We do not explicitly model the baryonic matter density profile (Fedeli 2014) because, on the scales of interest, its effect on the lensing signal can be approximated as that of a point mass (see Section 4.1). Because the lensing signal is measured by stacking galaxy groups with observable property $\mathcal{O}_{\mathrm{grp}}$, on scales smaller than the typical extent of a group, we have $P_{\mathrm{gm}}(k, z) = P_{\mathrm{grp\,m}}^{\mathrm{1h}}(k, z)$, where

$$P_{\mathrm{grp\,m}}^{\mathrm{1h}}(k, z) = \int \mathcal{P}(M|\mathcal{O}_{\mathrm{grp}}) \mathcal{H}_{\mathrm{m}}(k, M, z) \, \mathrm{d}M, \tag{20}$$

and

$$\mathcal{H}_{\mathrm{m}}(k, M, z) \equiv \frac{M}{\bar{\rho}_{\mathrm{m}}} \tilde{u}_{\mathrm{h}}(k|M, z), \tag{21}$$

with $\bar{\rho}_{\mathrm{m}}$ the comoving matter density of the Universe. Throughout the paper, the subscript 'grp' stands for 'galaxy group'.

The function $\mathcal{P}(M|\mathcal{O}_{\mathrm{grp}})$ is the probability that a group with observable property $\mathcal{O}_{\mathrm{grp}}$ resides in a halo of mass M. It reflects the halo occupation statistics and it can be written as

$$\mathcal{P}(M|\mathcal{O}_{\mathrm{grp}}) \, \mathrm{d}M = \mathcal{H}_{\mathrm{grp}}(M, z) \, n_{\mathrm{h}}(M, z) \, \mathrm{d}M. \tag{22}$$

Here, we have used

$$\mathcal{H}_{\mathrm{grp}}(M, z) \equiv \frac{\langle N \rangle_{\mathcal{O}_{\mathrm{grp}}}(M)}{\bar{n}_{\mathrm{grp}}(\mathcal{O}_{\mathrm{grp}}, z)}, \tag{23}$$

where, $\langle N \rangle_{\mathcal{O}_{\mathrm{grp}}}(M)$ is the average number of groups with observable property $\mathcal{O}_{\mathrm{grp}}$ that reside in a halo of mass M.

Note that $n_{\mathrm{h}}(M, z)$ is the halo mass function (i.e. the number density of haloes as a function of their mass) and we use the analytical function suggested in Tinker et al. (2008) as a fit to a numerical N-body simulation. Furthermore, the comoving number density of groups, $\bar{n}_{\mathrm{grp}}$, with the given observable property is defined as

$$\bar{n}_{\mathrm{grp}}(\mathcal{O}_{\mathrm{grp}}, z) = \int \langle N \rangle_{\mathcal{O}_{\mathrm{grp}}}(M) \, n_{\mathrm{h}}(M, z) \, \mathrm{d}M. \tag{24}$$

Note that in the expressions above, we have assumed that we can correctly identify the centre of the galaxy group halo (e.g. from the position of the galaxy identified as the central in the GAMA group catalogue). In Section 4.1, we generalize this expression to allow for possible *mis-centring* of the central galaxy.

Galaxy groups are not isolated, and on scales larger than the typical extent of a group, one expects a non-vanishing contribution to the power spectrum due to the presence of other haloes surrounding the group. This term is usually referred to as the two-halo term [as opposed to the one-halo term described in equation (20)]. One thus has

$$P_{\mathrm{gm}}(k) = P_{\mathrm{grp\,m}}^{\mathrm{1h}}(k) + P_{\mathrm{grp\,m}}^{\mathrm{2h}}(k). \tag{25}$$

These terms can be written in compact form as

$$P_{\mathrm{grp\,m}}^{\mathrm{1h}}(k, z) = \int \mathcal{H}_{\mathrm{grp}}(k, M, z) \mathcal{H}_{\mathrm{m}}(k, M, z) \, n_{\mathrm{h}}(M, z) \, \mathrm{d}M, \tag{26}$$

$$P_{\mathrm{grp\,m}}^{\mathrm{2h}}(k, z) = \int \mathrm{d}M_1 \, \mathcal{H}_{\mathrm{grp}}(k, M_1, z) \, n_{\mathrm{h}}(M_1, z)$$
$$\times \int \mathrm{d}M_2 \, \mathcal{H}_{\mathrm{m}}(k, M_2, z) \, n_{\mathrm{h}}(M_2, z) \, Q(k|M_1, M_2, z). \tag{27}$$

The quantity $Q(k|M_1, M_2, z)$ describes the power spectrum of haloes of mass M_1 and M_2. In its simplest implementation,[9] used throughout this paper, $Q(k|M_1, M_2, z) \equiv b_{\mathrm{h}}(M_1, z) b_{\mathrm{h}}(M_2, z) P^{\mathrm{lin}}(k, z)$, where $b_{\mathrm{h}}(M, z)$ is the halo bias function and $P^{\mathrm{lin}}(k, z)$ is the linear matter–matter power spectrum. We note that, in the literature, there exist various fitting functions to describe the mass dependence of the halo bias (see for example Sheth & Tormen 1999; Sheth, Mo & Tormen 2001; Tinker et al. 2010). These functions may exhibit differences of up to $\sim$10 per cent (e.g. Murray, Power & Robotham 2013). However, a few points are worth a comment.

First, the use of the fitting function from Tinker et al. (2010) is motivated by the use of a halo mass function calibrated over the same numerical simulation. Secondly, the halo bias function enters in the galaxy–matter power spectrum only through the two-halo term and as part of an integral. Thus, especially because we will fit the ESD profiles only up to $R = 2 \, h^{-1}\mathrm{Mpc}$, the uncertainty related to the halo bias function is much smaller than the statistical error associated with the observed signal.

4.1 Model specifics

The halo occupation statistics of galaxy groups are defined via the function $\langle N \rangle_{\mathcal{O}_{\mathrm{grp}}}(M)$, the average number of groups (with a

---

[8] We use M_{200} masses for the groups throughout this paper, i.e. as defined by 200 times the mean density (and corresponding radius, noted as R_{200}).

[9] See for example, van den Bosch et al. (2013) for a more refined description of this term.

given observable property $\mathcal{O}_{\rm grp}$, such as a luminosity bin) as a function of halo mass M. Since the occupation function of groups as a function of halo mass, $N_{\rm grp}(M)$, is either zero or unity, one has that $\langle N \rangle_{\mathcal{O}_{\rm grp}}(M)$ is by construction confined between zero and unity. We model $\langle N \rangle_{\mathcal{O}_{\rm grp}}(M)$ as a lognormal characterized by a mean, $\log[\tilde{M}/(h^{-1} M_\odot)]$, and a scatter $\sigma_{\log \tilde{M}}$:

$$\langle N \rangle_{\mathcal{O}_{\rm grp}}(M) \propto \frac{1}{\sqrt{2\pi}\,\sigma_{\log \tilde{M}}} \exp\left[-\frac{(\log M - \log \tilde{M})^2}{2\sigma_{\log \tilde{M}}^2} \right] . \tag{28}$$

We caution the reader against overinterpreting the physical meaning of this scatter; this number mainly serves the purpose of assigning a distribution of masses around a mean value.

Ideally, for each stack of the group ESD (in bins of group luminosity or total stellar mass) we wish to determine both these parameters, but to keep the number of fitting parameters low we assume here that $\sigma_{\log \tilde{M}}$ is constant from bin to bin, with a flat prior $0.05 \leq \sigma_{\log \tilde{M}} \leq 1.5$. This prior does not have any statistical effect on the results and it only serves the purpose of avoiding numerical inaccuracies. There is evidence for an increase in this parameter with central galaxy luminosity or stellar mass, (e.g. More et al. 2009a,b, 2011), but these increases are mild, and satellite kinematics (e.g. More et al. 2011) support the assumption that $\sigma_{\log \tilde{M}}$ is roughly constant on massive group scales (i.e. $\log [M/(h^{-1} M_\odot)] > 13.0$). We have verified that our assumption has no impact on our results in terms of either accuracy or precision by allowing $\sigma_{\log \tilde{M}}$ to be different in each observable bin.

For each given bin in an observable group property, one can define an effective mean halo mass, $\langle M \rangle$, as

$$\langle M \rangle_{\mathcal{O}_{\rm grp}} \equiv \int \mathcal{P}(M|\mathcal{O}_{\rm grp})\, M \, dM$$
$$= \frac{\int \langle N \rangle_{\mathcal{O}_{\rm grp}}(M)\, n_h(M, \bar{z}) M dM}{\bar{n}_{\rm grp}(\mathcal{O}_{\rm grp}, \bar{z})} , \tag{29}$$

where $\bar{z}$ is the mean redshift of the groups in the bin under consideration, and we have made use of equations (22) and (24). The effective mean halo mass, $\langle M \rangle_{\mathcal{O}_{\rm grp}}$, is therefore obtained as a weighted average where the weight is the multiplication of the halo occupation statistics and the halo mass function.

The dark matter density profile of a halo of mass M, $\rho_{\rm m}(r|M)$, is assumed to follow an NFW functional form

$$\rho_{\rm m}(r|M) = \frac{\bar{\delta}\,\bar{\rho}}{(r/r_{\rm s})(1 + r/r_{\rm s})^2} , \tag{30}$$

where $r_{\rm s}$ is the scale radius and $\bar{\delta}$ is a dimensionless amplitude which can be expressed in terms of the halo concentration parameter $c_{\rm m} \equiv R_{200}/r_{\rm s}$ as

$$\bar{\delta} = \frac{200}{3} \frac{c_{\rm m}^3}{\ln(1 + c_{\rm m}) - c_{\rm m}/(1 + c_{\rm m})} , \tag{31}$$

where the concentration parameter, $c_{\rm m}$, scales with halo mass. Different studies in the literature have proposed somewhat different fitting functions (e.g. Bullock et al. 2001; Eke, Navarro & Steinmetz 2001; Duffy et al. 2008; Macciò, Dutton & van den Bosch 2008; Klypin, Trujillo-Gomez & Primack 2011; Prada et al. 2012; Dutton & Macciò 2014) to describe the relation $c_{\rm m}(M, z)$. Overall, these studies are in broad agreement but unfortunately have not converged to a robust unique prediction. Given that those fitting functions have been calibrated using numerical simulations with very different configurations (most notably different mass resolutions and cosmologies), it remains unclear how to properly account for the above mentioned discrepancies. As these fitting functions

all predict a weak mass dependence, we decide to adopt an effective concentration–halo mass relation that has the mass and redshift dependence proposed in Duffy et al. (2008) but with a rescalable normalization:

$$c_{\rm m}^{\rm eff}(M_{200}, z) = f_{\rm c} \times c_{\rm m}^{\rm Duffy}(M_{200}, z)$$
$$= f_{\rm c} \times 10.14 \left(\frac{M_{200}}{2 \times 10^{12}} \right)^{-0.081} (1 + z)^{-1.01}. \tag{32}$$

Note that at $z = 0.25$, one has $c_{\rm m}^{\rm Duffy} \approx 5$ for halo masses with $\log [M/(h^{-1} M_\odot)] \approx 14.3$. We leave $f_{\rm c}$ free to vary within a flat uninformative prior $0.2 \leq f_{\rm c} \leq 5$.

The innermost part of a halo is arguably the site where a 'central' galaxy resides. The baryons that constitute the galaxy may be distributed according to different profiles depending on the physical state (for example, exponential discs for stars and β-profiles for hot gas; see Fedeli 2014). The lensing signal due to these different configurations could in principle be modelled to a certain level of sophistication (see Kobayashi et al. 2015). However, at the smallest scales of interest here,[10] those distributions might as well be accounted for by simply assuming a point mass, $M_{\rm P}$. In the interest of simplicity, we assume that the stellar mass of the brightest cluster galaxy ($M_\star^{\rm BCG}$; Taylor et al. 2011) is a reliable proxy for the amount of mass in the innermost part of the halo. Specifically, we assume that

$$M_{\rm P} = A_{\rm P} M_\star^{\rm BCG} , \tag{33}$$

where $A_{\rm P}$ is a free parameter, within a flat prior between 0.5 and 5.

The adopted definition of centre may well differ from the true minimum of the gravitational potential well. Such a mis-centring of the 'central' galaxy is in fact seen in galaxy groups (see e.g. Skibba & Macciò 2011 and references therein). George et al. (2012) offer further independent support of such a mis-centring, finding that massive central galaxies trace the centre of mass to less than 75 kpc h^{-1}.

We model this mis-centring in a statistical manner (see also Oguri & Takada 2011; Miyatake et al. 2015; More et al. 2015 and references therein). Specifically, we assume that the degree of mis-centring of the groups in three dimensions, $\Delta(M, z)$, is proportional to the halo scale radius $r_{\rm s}$, a function of halo mass and redshift, and parametrize the probability that a 'central' galaxy is mis-centred as $p_{\rm off}$. This gives

$$\mathcal{H}_{\rm grp}(k, M, \bar{z}) = \frac{\langle N \rangle_{\mathcal{O}_{\rm grp}}(M)}{\bar{n}_{\rm grp}(\bar{z})} (1 - p_{\rm off} + p_{\rm off} \times e^{[-0.5 k^2 (r_{\rm s} \mathcal{R}_{\rm off})^2]}). \tag{34}$$

Setting either $p_{\rm off}$ or $\mathcal{R}_{\rm off}$ to zero implies that there is de facto no offset. We treat the two as free parameters in Section 5. The parameter $p_{\rm off}$, being a probability, is bound between zero and unity. We apply a flat uniform prior to $\mathcal{R}_{\rm off} \in [0, 1.5]$. We note that this prior is very conservative, as according to George et al. (2012) and Skibba & Macciò (2011) the mis-centring is expected to be smaller than the scale radius of a group, for which $\mathcal{R}_{\rm off} = 1$.

In summary, the model parameter vector, is defined as $\lambda = (\log\tilde{M}_i, \sigma_{\log\tilde{M}}, f_{\rm c}, A_{\rm P}, p_{\rm off}, \mathcal{R}_{\rm off})$ where $i = 1, \ldots, N_{\rm bins}$. Throughout the paper, we bin group observable properties in six bins. This leads to an 11-parameter model. We use Bayesian inference techniques to determine the posterior probability distribution $P(\lambda|\mathcal{D})$ of the model parameters given the data, $\mathcal{D}$. According to Bayes'

[10] We fit the data in the range $0.02 < R/(h^{-1} {\rm Mpc}) < 2.0$.

Table 2. Summary of the bin limits used to compute the stacked ESD signal, the number of groups in each bin, the mean redshift of the groups in each bin and the mean stellar mass of the BCG.

Observable	Bin limits	Number of lenses	Mean redshift	$\log(\langle M_\star^{\mathrm{BCG}}[h^{-2}\,\mathrm{M_\odot}]\rangle)$
$\log[L_{\mathrm{grp}}/(h^{-2}\,\mathrm{L_\odot})]$	(9.4, 10.9, 11.1, 11.3, 11.5, 11.7, 12.7)	(540, 259, 178, 233, 142, 66)	(0.13, 0.20, 0.23, 0.26, 0.30, 0.35)	(11.00, 11.23, 11.29, 11.37, 11.47, 11.70)
$\sigma/(\mathrm{s^{-1}km})$	(0, 225, 325, 375, 466, 610, 1500)	(501, 359, 124, 198, 147, 89)	(0.15, 0.19, 0.21, 0.23, 0.26, 0.31)	(11.05, 11.20, 11.30, 11.36, 11.41, 11.64)
N_{fof}	(5, 6, 7, 8, 11, 19, 73)	(481, 261, 170, 239, 181, 86)	(0.21, 0.21, 0.21, 0.19, 0.18, 0.16)	(11.17, 11.23, 11.29, 11.29, 11.35, 11.45)
$L_{\mathrm{BCG}}/L_{\mathrm{grp}}$	(1.0, 0.35, 0.25, 0.18, 0.13, 0.08, 0)	(346, 252, 296, 227, 200, 97)	(0.10, 0.16, 0.20, 0.25, 0.29, 0.34)	(11.16, 11.19, 11.22, 11.29, 11.36, 11.53)

theorem,

$$P(\lambda|\mathcal{D}) \propto P(\mathcal{D}|\lambda)\, P(\lambda) \propto \exp\left[\frac{-\chi^2(\lambda)}{2}\right]\, P(\lambda), \qquad (35)$$

where $P(\mathcal{D}|\lambda)$ is the likelihood of the data given the model parameters, assumed to be Gaussian, and $P(\lambda)$ is the prior probability of these parameters. Here,

$$\chi^2(\lambda) = [\widetilde{\Delta\Sigma}_{k,j} - \Delta\Sigma_{k,j}]^T (\mathbf{C}^{-1})_{kk',jj'} [\widetilde{\Delta\Sigma}_{k',j'} - \Delta\Sigma_{k',j'}], \quad (36)$$

where $\Delta\Sigma_{k,j}$ is the j'th radial bin of the observed stacked ESD for the groups in bin k, and $\widetilde{\Delta\Sigma}_{k,j}$ is the corresponding model prediction. $\mathbf{C}$ is the full covariance matrix for the measurements, computed as detailed in Section 3.4.

We sample the posterior distribution of our model parameters given the data using a Markov Chain Monte Carlo (MCMC). In particular, we use[11] a proposal distribution that is a multivariate Gaussian whose covariance is computed via a Fisher analysis run during the burn-in phase of the chain, set to 5000 model evaluations.

5 DENSITY PROFILE OF GALAXY GROUPS

We measure the ESD signal around each GAMA group with at least five members in 10 logarithmically-spaced radial bins in the range $20\,h^{-1}\,\mathrm{kpc}$–$2\,h^{-1}\,\mathrm{Mpc}$. We first assign errors to those measurements by propagating the shape noise on the tangential shear measurement in each radial bin. We divide the groups into six bins according to a given observable property, such as their velocity dispersion, total r-band luminosity, apparent richness or r-band luminosity fraction of the BCG. Bin limits are chosen to make the signal to noise of the ESD roughly the same in each bin. Once the bin limits are defined, we compute the data covariance between radial bins and between group bins as outlined in Section 3.4. We summarize the bin-limits, the number of groups in each bin, the mean redshift of the bin and the mean stellar mass of the BCG in Table 2 for the four observables considered in this work.

The typical signal-to-noise ratio in each of the six luminosity bins is of the order of $\sim$20–25. This is comparable to the signal-to-noise ratio reported by Sheldon et al. (2009) for a weak lensing analysis of $\sim$130 000 MaxBCG clusters using SDSS imaging, once we restrict the comparison to a similar luminosity range.

We jointly fit the signal in the six bins using the halo model described in Section 4. Since GAMA is a flux limited survey, the redshift distributions of the groups in the six luminosity bins are different, as shown in Fig. 6. When we fit the halo model to the data, we calculate the power spectra and mass function (equations 20–27) using the median of the redshift distribution in each bin.

For each observable property, we run five independent chains with different initial conditions. We evaluate the convergence of the
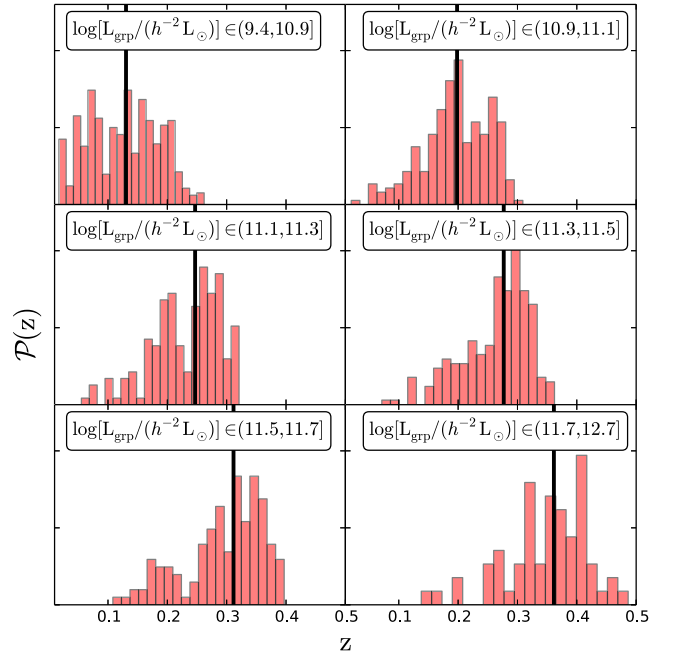
Figure 6. Redshift distributions of the GAMA groups used in this paper in the six r-band luminosity bins. The group luminosity increases from left to right and from top to bottom. The solid vertical black lines indicate the median of the distributions.

MCMC by means of a Gelman Rubin test (Gelman & Rubin 1992), and we impose $R < 1.03$, where the R-metric is defined as the ratio of the variance of a parameter in the single chains to the variance of that parameter in an '*über-chain*', obtained by combining five chains.

5.1 Matter density profiles of group-scale haloes

We first test whether the ESD measurements themselves support the halo model assumption that the group density profile can be described in terms of a mis-centred NFW profile with a contribution from a point mass at small scales, and what constraints can be put on the model parameters. In the interest of being concise, we only present the results derived by binning the groups according to their total r-band luminosity (see Section 3), as statistically equivalent results are obtained when the groups are binned according to their velocity dispersion, apparent richness or r-band luminosity fraction of the BCG. The binning by other observables will become important in the study of scaling relation presented in Section 6.

One needs to define the centre of the halo before stacking the ESD profiles of the groups. Following R+11, we have three choices for the group centre: the centre of light (Cen), the Brightest Cluster Galaxy (BCG) and the brightest galaxy left after iteratively removing the most distant galaxies from the group centre of light (IterCen).

---

[11] A python implementation of this sampling method is available via the MONTEPYTHON code thanks to the contribution by Surhud More.
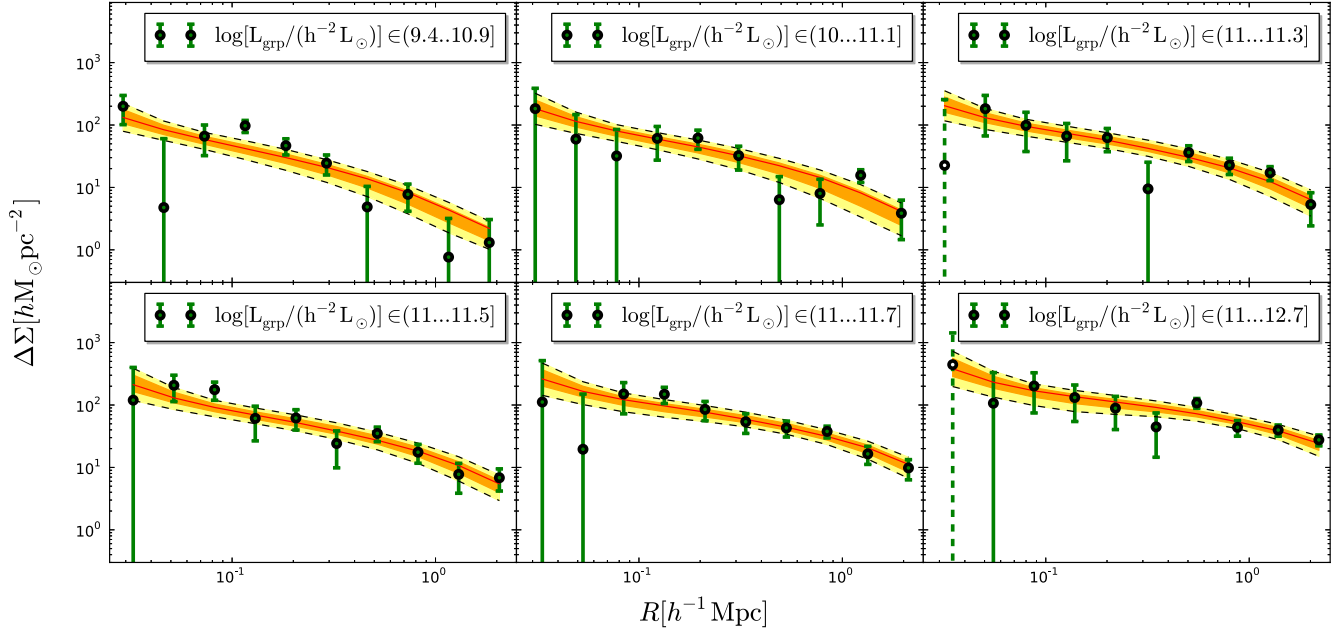
Figure 7. Stacked ESD profile measured around the groups BCG of the six group luminosity bins as a function of distance from the group centre. The group *r*-band luminosity increases from left to right and from top to bottom. The stacking of the signal has been done using only groups with $N_{\rm fof} \geq 5$. The error bars on the stacked signal are computed as detailed in Section 3.4 and we use dashed bars in the case of negative values of the ESD. The orange and yellow bands represent the 68 and 95 percentile of the model around the median, while the red line shows the best-fitting model.

Throughout the paper, unless stated otherwise, we use the BCG as the definition of the centre, as it is a common choice in the literature. We investigate the effect of using the other two definitions of the group centre in Section 5.1.4 and in Appendix A.

Fig. 7 shows the stacked ESD profiles (green points with error bars) for the six bins in total *r*-band luminosity. Note that the error bars are the square root of the diagonal elements of the full covariance matrix, and we use dashed bars in the case of negative values of the ESD. The ESD profiles have high signal to noise throughout the range in total luminosity and in spatial scales. Red lines indicate the best-fitting model, whereas orange and yellow bands indicate the 68 and 95 per cent confidence interval. The model describes the data well with a reduced $\chi^2_{\rm red} = 1.10$, 49 d.o.f., over the full scale range, for all the luminosity bins. This justifies our assumption that the ESD profile can be accurately modelled as a weighted stack of mis-centred NFW density profiles with a contribution from a point mass at the centre.

The main results of this analysis can be summarized as follows (68 per cent confidence limits quoted throughout).

(i) For each *r*-band luminosity bin, we derive the probability that a group with that luminosity resides in a halo of mass *M* (see equation 22). We show the median of the probability distribution for the six bins in Fig. 8. We constrain the scatter in the mass at a fixed total *r*-band luminosity to be $\sigma_{\log \tilde{M}} = 0.74^{+0.09}_{-0.16}$. This sets the width of the lognormal distribution describing the halo occupation statistics. We remind the reader that $\sigma_{\log \tilde{M}}$ is the width of the distribution in halo masses at given total luminosity of the groups and it is *not* the scatter in luminosity (or stellar mass) at a fixed halo mass that is often quoted in the literature and that one would expect to be considerably smaller (e.g. Cacciato et al. 2009; Yang, Mo & van den Bosch 2009; More et al. 2011; Leauthaud et al. 2012a). This hampers the possibility of a one-to-one comparison with most studies in the literature. However, we note that van den Bosch et al. (2007) and More et al. (2011) reported values of the
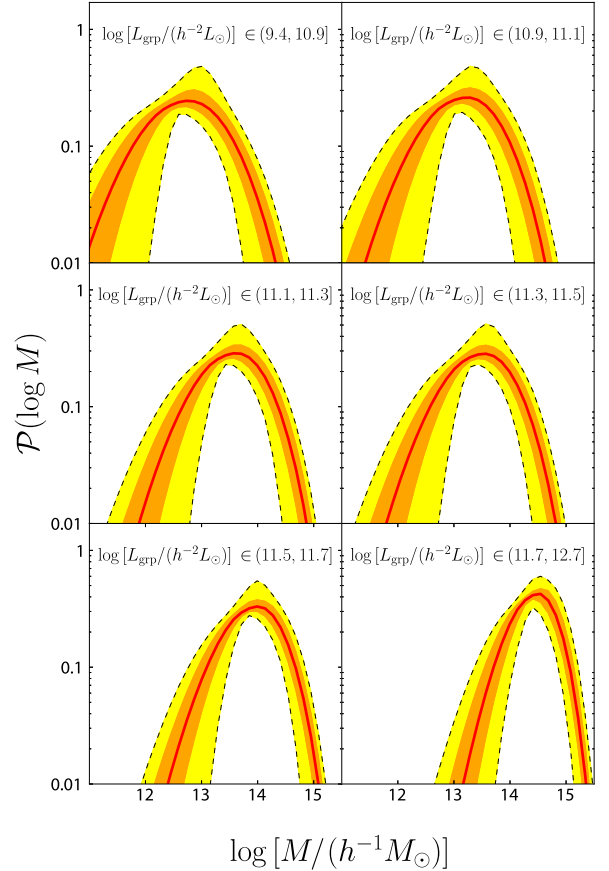

Figure 8. Probability that a group with a given *r*-band luminosity resides in a halo of mass *M*. The red lines show the median distribution, while the orange and the yellow contours show the 68 and 95 percentile around the median.
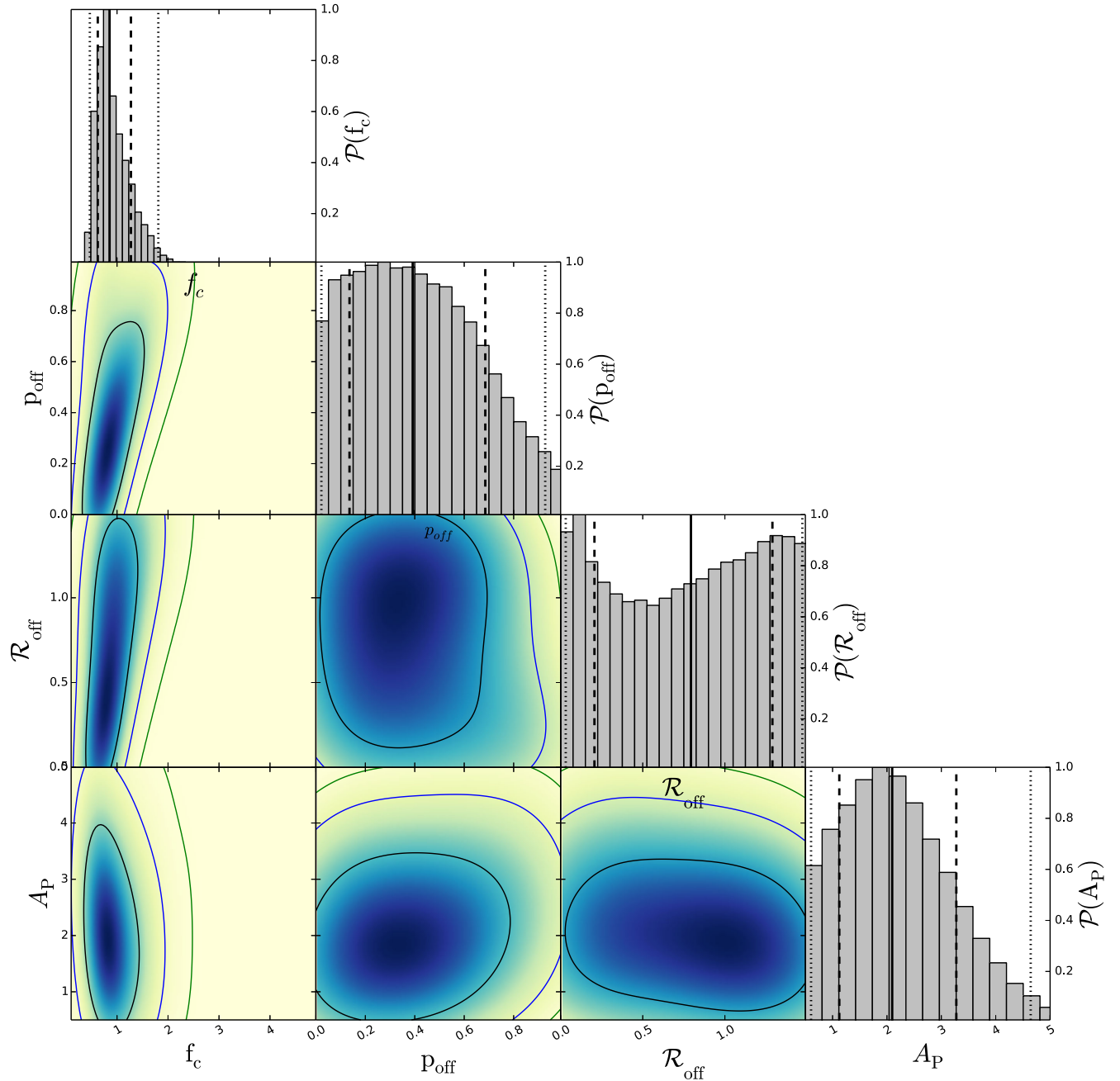
Figure 9. Posterior distribution of the normalization of the mass-concentration relation f_c, of the mis-centring parameters p_{off} and $\mathcal{R}_{off}$ and of the amplitude of the point mass A_P. The contours indicate the 1σ, 2σ, 3σ confidence regions. The dashed vertical lines and the dotted vertical lines correspond, respectively, to the 1σ and 2σ marginalized confidence limits .These are the constraints from a joint halo model fit of the ESD signal in the six luminosity bins using BCG as the group centre. The range in each panels reflect the priors used for the different parameters.

scatter in halo mass at fixed luminosity that are as high as 0.7 at the bright end. Furthermore, More et al. (2015) reported a value of $0.79^{+0.41}_{-0.39}$ for the width of the low-mass end distribution of the halo occupation statistics of massive CMASS galaxies. Given the non-negligible differences between the actual role of this parameter in all these studies, we find this level of agreement satisfactory.

(ii) For each luminosity bin, a mean halo mass is inferred with a typical uncertainty on the mean of ~ 0.12 dex.

(iii) The relative normalization of the concentration–halo mass relation (see equation 32) is constrained to be $f_c = 0.84^{+0.42}_{-0.23}$, in agreement with the nominal value based on Duffy et al. (2008).

(iv) The probability of having an off-centred BCG is $p_{off} < 0.97$ (2σ upper limit), whereas the average amount of mis-centring in terms of the halo scale radius, $\mathcal{R}_{off}$, is unconstrained within the prior.

(v) The amount of mass at the centre of the stack which contributes as a point mass to the ESD profiles is constrained to be $M_{PM} = A_{PM} \langle M_{\star}^{BCG} \rangle = 2.06^{+1.19}_{-0.99} \langle M_{\star}^{BCG} \rangle$.

Fig. 9 shows the posterior distributions of the halo model parameters and their mutual degeneracies. Tables 3 and 4 list the median values of the parameters of interest with errors derived from the 16th and

Table 3. Constraints on the average halo mass in each *r*-band luminosity bin using the three definitions of halo centre. We quote here the median of the mass posterior distribution, marginalized over the other halo model parameters, and the errors are the 16th and 84th percentile of the distribution. All of the constraints derived using the three different proxies for the halo centre agree within 1σ.

Centre	$\log[M_{200}^{(1)}/(h^{-1}\mathrm{M_\odot})]$	$\log[M_{200}^{(2)}/(h^{-1}\mathrm{M_\odot})]$	$\log[M_{200}^{(3)}/(h^{-1}\mathrm{M_\odot})]$	$\log[M_{200}^{(4)}/(h^{-1}\mathrm{M_\odot})]$	$\log[M_{200}^{(5)}/(h^{-1}\mathrm{M_\odot})]$	$\log[M_{200}^{(6)}/(h^{-1}\mathrm{M_\odot})]$
BCG	$13.15^{+0.13}_{-0.15}$	$13.52^{+0.13}_{-0.15}$	$13.83^{+0.11}_{-0.12}$	$13.76^{+0.10}_{-0.12}$	$14.13^{+0.09}_{-0.10}$	$14.55^{+0.10}_{-0.10}$
IterCen	$13.21^{+0.12}_{-0.13}$	$13.45^{+0.13}_{-0.16}$	$13.76^{+0.11}_{-0.13}$	$13.77^{+0.10}_{-0.11}$	$14.16^{+0.08}_{-0.09}$	$14.53^{+0.09}_{-0.09}$
Cen	$13.00^{+0.17}_{-0.23}$	$13.64^{+0.12}_{-0.16}$	$13.92^{+0.10}_{-0.12}$	$13.85^{+0.10}_{-0.12}$	$14.18^{+0.09}_{-0.10}$	$14.64^{+0.10}_{-0.10}$

Table 4. Constraints on the halo model parameters using the three definitions of halo centre. For each of the parameters, we quote the median of the posterior distribution, marginalized over the other parameters, while the errors are the 16th and 84th percentile of the distribution. All the constraints derived using the three different proxies for the halo centre agree within 1σ.

Centre	$\sigma_{\log[\tilde{M}]}$	$f_{\rm c}$	$p_{\rm off}$	$\mathcal{R}_{\rm off}$	$A_{\rm P}$
BCG	$0.74^{+0.09}_{-0.16}$	$0.84^{+0.42}_{-0.23}$	$0.38^{+0.30}_{-0.27}$	$0.79^{+0.52}_{-0.62}$	$2.06^{+1.19}_{-0.99}$
IterCen	$0.74^{+0.10}_{-0.16}$	$0.94^{+0.43}_{-0.23}$	$0.37^{+0.27}_{-0.26}$	$0.87^{+0.46}_{-0.65}$	$1.76^{+1.12}_{-0.87}$
Cen	$0.67^{+0.10}_{-0.17}$	$1.10^{+0.32}_{-0.46}$	$0.98^{+0.02}_{-0.09}$	$1.00^{+0.37}_{-0.51}$	$0.91^{+0.63}_{-0.33}$

84th percentiles of the posterior distribution. We discuss the constraints on the model parameters in further detail in the remainder of this section.

5.1.1 Masses of dark matter haloes

The dark matter halo masses of the galaxy groups that host the stacked galaxy groups analysed in this work span one and a half orders of magnitude with $M \in [10^{13} \ldots 10^{14.5}] \, h^{-1} \, \mathrm{M_\odot}$. Since our ESD profiles extend to large radii, our $2 \, h^{-1}$ Mpc cut-off is larger than R_{200} over this full mass range, these mass measurements are robust and direct as they do not require any extrapolation. The uncertainties on the masses are obtained after marginalising over the other model parameters. Typically these errors are 15 per cent larger than what would be derived by fitting an NFW profile to the same data, ignoring the scatter in mass inside each luminosity bins. Note that a simple NFW fit to the data in the six luminosity bins, with fixed concentration (Duffy et al. 2008) would also lead to a bias in the inferred masses of approximately 25 per cent.

The inferred halo masses in each luminosity bin are slightly correlated due to the assumption that the scatter in halo mass is constant in different bins of total luminosity. We compute the correlation between the inferred halo masses from their posterior distribution, and we show the results in Fig. 10. Overall, the correlation is at most 20 per cent, and this is accounted for when deriving scaling relations (see Section 6).

5.1.2 Concentration and mis-centring

The shape of the ESD profile at scales smaller than $\sim 200 \, h^{-1}$ kpc contains information on the concentration of the halo and on the mis-centring of the BCG with respect to the true halo centre. However, the relative normalization of the concentration–halo mass relation, $f_{\rm c}$, and the two mis-centring parameters, $p_{\rm off}$ and $\mathcal{R}_{\rm off}$ are degenerate with each other. A small value of $f_{\rm c}$ has a similar effect on the stacked ESD as a large offset: both flatten the profile. To further illustrate this degeneracy, we show in Fig. 11 the 2D posterior distribution of the average projected offset ($p_{\rm off} \times \mathcal{R}_{\rm off}$)
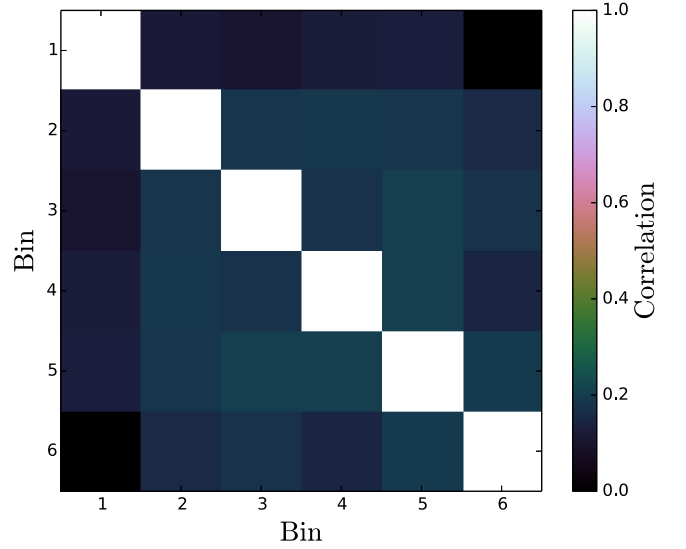

Figure 10. Correlation matrix between the mean halo masses derived in the six *r*-band luminosity bins from the halo model fit. The reason for the correlation is the assumption of a constant scatter as a function of group luminosity in the halo occupation distribution.
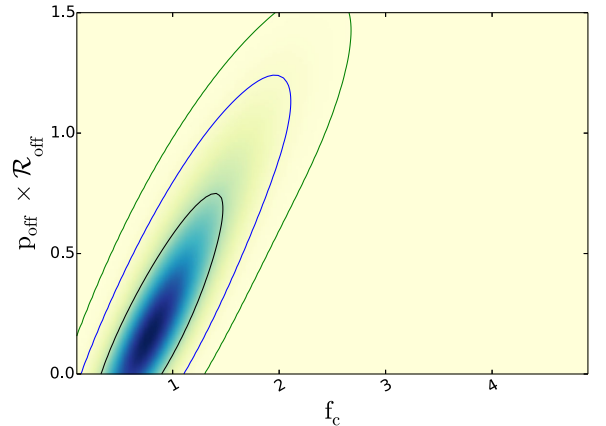

Figure 11. 2D posterior distribution of the average projected offset ($p_{\rm off} \times \mathcal{R}_{\rm off}$) and the normalization of the concentration–halo mass relation $f_{\rm c}$. The contours indicate the 68, 95, and 99 per cent confidence region.

and the normalization of the concentration–halo mass relation. It is clear how a vanishing offset would require a low value of the concentration.

The derived constraints on the average projected BCG offset are quite loose: $p_{\rm off} \times \mathcal{R}_{\rm off} < \infty.\infty / \nabla_{\rm s}$ (2σ). Hence one might argue in favour of a simpler model or a model with a less informative prior on $\mathcal{R}_{\rm off}$. We address both aspects in the following ways. First,
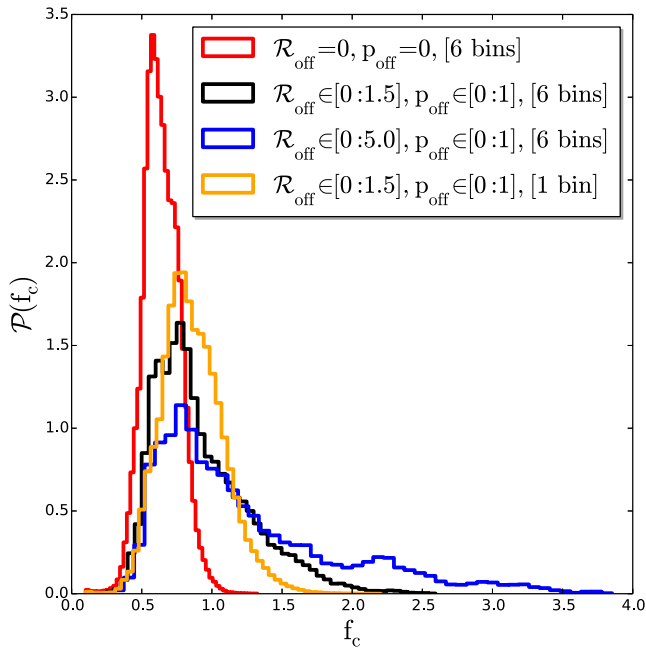
Figure 12. Posterior distribution for the normalization of the mass–concentration relation (Duffy et al. 2008) after marginalizing over the other model parameters. We show here the effect of changing the prior in the mis-centring parameters: $\mathcal{R}_{\mathrm{off}} = 0$ (red line), $\mathcal{R}_{\mathrm{off}} \in [0, \ldots, 1.5]r_s$ (black line) and $\mathcal{R}_{\mathrm{off}} \in [0, \ldots, 5]r_s$ (blue line). As a reference, the orange line shows the posterior distribution for f_c in the case of a global stack of all groups. This has to be compared with the black line, where the constraints were derived from a joint fit of the stacked ESD in six luminosity bins.

we run a version of the halo model on the same six luminosity bins in which we assume no mis-centring (i.e. we assume that the BCG is always at the centre of the dark matter halo). We find a similar value of the reduced chi-squared ($\chi^2_{\mathrm{red}} = 1.04$, 51 d.o.f.), comparable values for the six masses (always within one sigma) but tighter constraints for the relative normalization of the concentration–halo mass relation, $f_c = 0.59^{+0.13}_{-0.11}$. This is perhaps not entirely surprising given that in this case f_c is not degenerate with any other model parameter. Secondly, we relax the prior for $\mathcal{R}_{\mathrm{off}}$ from $0 \le \mathcal{R}_{\mathrm{off}} \le 1.5$ to $0 \le \mathcal{R}_{\mathrm{off}} \le 5$. Also in this case, we find statistically equivalent halo masses and similar constraints on p_{off}, $\mathcal{R}_{\mathrm{off}}$, and f_c as in the fiducial case. We summarize the results of these tests in Fig. 12. We conclude that the fact that the reduced χ^2 values for the three model-configurations are very similar and always larger than unity suggests that the 11-parameter model is not too complex given the signal to noise of the data. Ignoring the mis-centring in the model lowers the relative normalization of the concentration–halo mass relation to a 3σ deviation from the nominal value of Duffy et al. (2008). However, we caution the reader against overinterpreting this result as our test shows that this is probably driven by the very strong prior on the location of the BCGs rather than actually being a physical property of the stacked haloes.

Lower values of the normalization of the concentration–halo mass relation from weak lensing analysis have been previously reported. For example, Mandelbaum, Seljak & Hirata (2008) studied a sample of LRGs and MaxBCG clusters from SDSS and reported a 2σ deviation of the normalization of the mass–concentration relation with respect to the simulation predictions. In this case, the lenses were assumed to be the true centre of the dark matter halo, and the analysis limited to scales larger than $0.5\ h^{-1}$ Mpc to limit the impact of mis-

centring. From a weak lensing and clustering analysis of SDSS-III CMASS galaxies, Miyatake et al. (2015) also found a lower normalization if mis-centring of the lenses is not included in the model but report agreement with the theoretical predictions once the mis-centring is included. A similar conclusion was derived by van Uitert et al. (2015) from a lensing analysis of LOWZ and CMASS LRGs from the Baryon Oscillation Spectroscopic Survey (BOSS) SDSS-DR10 using imaging data from the second Red-sequence Cluster Survey. In an analysis of the CFHT Stripe 82 Survey for haloes of masses around $10^{14}\ h^{-1}\ \mathrm{M}_\odot$, Shan et al. (2015) also reported a nominal value of the normalization of the concentration–halo mass relation lower than the Duffy et al. (2008) prediction, but the discrepancy between observations and predictions from numerical simulations was not statistically significant.

Possible explanations for a lower normalization of the concentration–halo mass relation might include halo-triaxiality, which we do not account for in our model, substructures inside the main halo (Giocoli et al. 2012), galaxy formation related processes which can make halo density profiles shallower by expelling baryons into the outer region of the halo (Sales et al. 2010; van Daalen et al. 2011) and the assumed cosmological model. In fact, the value of the concentration at a given redshift, as a measure of the formation time of haloes, depends on the background cosmology. To address this last point, we run the halo model assuming two alternative cosmologies: a slight deviation from the nominal Planck result ($\Omega_{\mathrm{m}}, \sigma_8, h, n_s, \Omega_{\mathrm{b}} h^2$) = (0.302, 0.818, 0.68, 0.9686, 0.02197) (Spergel, Flauger & Hložek 2015), and the best-fitting result of a clustering and lensing analysis on SDSS data ($\Omega_{\mathrm{m}}, \sigma_8, h, n_s, \Omega_{\mathrm{b}} h^2$) = (0.278, 0.763, 0.739, 0.978, 0.02279) (Cacciato et al. 2013), which we regard as an extreme change in light of the recent Planck results. We do not find any difference in the posterior distributions of any model parameters, in particular on f_c. We hence conclude that our results are not affected by the assumed cosmology.

5.1.3 Point mass: the innermost part of the halo

Measurements of the ESD profile at scales smaller than $\sim 50\ h^{-1}$ kpc constrain the amount of mass at the centre of the halo. We model this as a simple point mass. The measured amplitude of the point mass is not degenerate with any of the other halo model parameters, demonstrating that, given the quality of the data, the details of the distribution of the baryons at the very centre of the haloes are not relevant to infer global properties of the dark matter halo, such as their masses or concentrations.

5.1.4 Other definitions of the group centre

Finally, we repeat the analysis using two alternative definitions of the group centre in the GAMA catalogue: the centre of light (Cen) and the brighter galaxy left after iteratively removing the most distant galaxy from the group centre of light (IterCen). We present the results in Appendix A, Tables 3 and 4. We do not find any significant difference in the ESD profile when using IterCen instead of the BCG. However, the profile is very different when we use Cen. In this case, we find tight constraints on the probability of the centre of light of not being the centre of the dark matter halo with $p_{\mathrm{off}} \ge 0.67$ at 2σ and we find that on average the amount of mis-centring of the centre of light with respect to the minimum of the halo potential well is $\mathcal{R}_{\mathrm{off}} = 1.00^{+0.37}_{-0.51}$. The constraints on the halo masses in the six luminosity bins, as well as the constraints on $\sigma_{\log \bar{M}}$, f_c, and A_{P}, are however consistent within 1σ with those calculated using the BCG position.
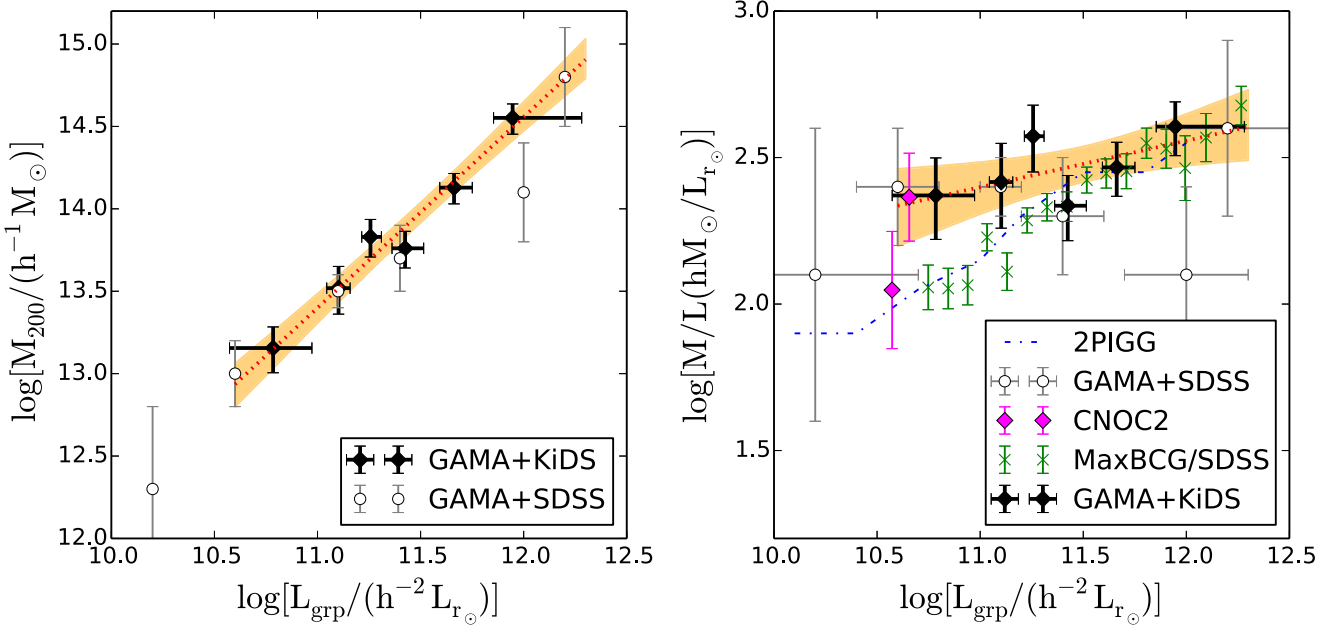
Figure 13. Left panel: halo mass as a function of the total group *r*-band luminosity. The solid black points show the halo masses derived in this work from a halo model fit to the stacked ESD profile of groups with at least five members brighter than the GAMA magnitude limit. The vertical error bars indicate the 1σ uncertainty on the average halo mass after marginalizing over the other halo model parameters, while the horizontal error bars indicate the 16th and 84th percentile of the luminosity distribution in each bin. The red line shows the best-fitting power-law to the data points, while our estimate of the 1σ dispersion around this relation is shown as the orange area (see text). The open black circles show the halo masses derived from a lensing analysis of GAMA groups using SDSS galaxies as background sources (Han et al. 2015). Right panel: derived mass-to-light ratio as a function of the group total luminosity from this work (black points), from the GAMA+SDSS analysis (open black circles), from the analysis of the CNOC2 group sample (Parker et al. 2005) (magenta diamonds) and from a lensing analysis of 130 000 groups from the MaxBCG catalogue using SDSS imaging (Sheldon et al. 2009, (green crosses)). In blue, we show the median relation derived using the 2PIGG catalogue (Eke et al. 2004). The red lines and the orange area correspond to those of the left-hand panel.

In summary, our results highlight the importance of a proper model for the mis-centring in the analysis of the ESD signal from groups or clusters of galaxies. Neglecting it could lead to biases in the derived parameters, particularly the normalization of the concentration–mass relation.

6 SCALING RELATIONS

In the last section of this paper, we investigate the correlations between the halo masses derived using weak gravitational lensing and optical properties of galaxy groups measured from SDSS images and the GAMA catalogue (R+11). There are two main reasons to study these scaling relations: (i) to understand which physical processes take place inside galaxy groups and their impact on galaxy formation; (ii) to constrain a mean relation, as well as the scatter, between some observable property of the groups and their halo mass for use in cosmological analyses that rely on the halo mass function.

6.1 The relation between halo mass and group *r*-band luminosity

We first investigate the scaling relation between the total halo mass and the total *r*-band luminosity of the groups. As described in the previous section, we bin the groups according to their total *r*-band luminosity (see Table 2), fit a halo model to the stacked ESDs, and record the halo mass posteriors for each bin. We show the results, halo mass a function of group luminosity, in the left-hand panel of Fig. 13.

We fit a power-law relation between the halo mass and the total *r*-band luminosity of the group:

$$\frac{M_{200}}{10^{14}h^{-1}\,\mathrm{M_\odot}} = (0.95 \pm 0.14)\left(\frac{L_{\mathrm{grp}}}{10^{11.5}\,h^{-2}\,\mathrm{L_\odot}}\right)^{(1.16\pm0.13)}. \quad (37)$$

The linear regression is performed in the log-basis, since the errors on the masses are lognormal distributed, by minimizing the offset of the mass measurements from the power-law relation. We explicitly account for the correlation between halo masses (see Section 5). The red line in Fig. 13 shows the best-fitting relation. Our estimate of the 1σ dispersion around this relation is shown as the orange band and is derived from the joint posterior distributions for the halo masses from five independent MCMCs. We jointly extract 10^5 random values of the masses in each of the six *r*-band luminosity bins (in order to preserve the correlation between the masses), and we fit a linear relation to each log-mass vector as a function of the logarithm of the *r*-band luminosity. Finally, we compute the 16th and 84th percentiles of the best-fitting models in the different *r*-band luminosity bins. The average logarithmic scatter in halo mass at fixed *r*-band luminosity is $\sigma_{\log\langle M_{200}\rangle} = 0.17$

In the left-hand panel of Fig. 13, we also compare our results to a previous weak lensing analysis of the same group catalogue (open black points) that used SDSS galaxies as background sources (Han et al. 2015). That analysis included all groups with $N_{\mathrm{fof}} \geq 3$ and fitted a single maximum likelihood mass to all the galaxies within a number of *r*-band luminosity bins. The agreement between the two analyses is remarkable given the different quality of data and

the different techniques used to infer the halo masses. Nevertheless, we stress that the current analysis based on the first KiDS data not only yields some of the tightest lensing constraints on group masses to date but also does this whilst marginalizing over halo model parameters not considered in the previous work.

Mock simulations suggest that the GAMA group catalogue is significantly contaminated by chance projections for groups with two and three members and marginally contaminated for groups with four members. Thus, while the only way to obtain constraints on low-luminosity systems ($L_{grp} \lesssim 10^{10.5} \, L_\odot \, h^{-2}$) is to include such sparse groups in the analysis, the impurity of the selection makes any results on the average mass of such groups unreliable and difficult to quantify (most likely underestimated). Our lowest luminosity bin may suffer from a bias due to this same richness criterion if, as seems plausible, the poorer groups that are not included at a given luminosity have systematically lower masses.

According to our current understanding of galaxy formation, one would expect the slope of the mass–luminosity relation to change towards the low-mass end, for haloes of about 10^{12}–$10^{13} \, M_\odot \, h^{-1}$. This is mostly due to star formation being most efficient in haloes of $\sim 10^{12} \, h^{-1} \, M_\odot$ (see for example Behroozi, Wechsler & Conroy 2013, and references therein), implying the dominant feedback process is mass ejection from supernovae (see e.g. Dekel & Silk 1986). However, we are only able to probe the mass–luminosity relation for haloes more massive than about $10^{13} \, M_\odot \, h^{-1}$. In the regime modelled here, the relation is well fitted by a single power law.

The right-hand panel of Fig. 13 shows the relation between halo mass and total r-band luminosity in terms of the mass-to-light ratio. The mass-to-light ratio is relatively constant with total group r-band luminosity, with a slight increase of less than 0.1 dex from the lowest to the highest luminosity bin. The scatter around this ratio is as large as 0.2 dex. Ideally, one would like to compare this result with previous results from the literature. Unfortunately, different authors use different definitions of halo masses, group luminosities are often measured in different bands, and group selection functions might differ due to different survey depths or different algorithms used to identify groups. This might easily lead to different scaling relations, and we would like to highlight to the reader that a face-value comparison might be misleading. Despite these uncertainties, we qualitatively compare our results with previous measurements in what follows.

One of the first analyses of a large sample of groups was based on the 2dFGRS, using a percolation technique to identify groups while also allowing dynamical mass measurements (Eke et al. 2004). The group luminosity was measured both in b_J and r_F band. We show this result as the blue line in the right-hand panel of Fig. 13. We find a qualitatively similar trend of the mass-to-light ratio as a function of the total group r-band luminosity for $L_{grp} > 10^{11} L_{r_\odot} \, h^{-2}$. However, our data do not support the steep increase of the mass-to-light ratio in the range $10^{10} L_{r_\odot} \, h^{-2} < L_{grp} < 10^{11} L_{r_\odot} \, h^{-2}$ reported by Eke et al. (2004).

Han et al. (2015) carried out a detailed comparison between their results (which are in agreement with the one presented in this work) and the results from Eke et al. (2004), concluding that the steep increase in the mass-to-light ratio observed in the 2dF-GRS sample could be mostly explained by the different depth between 2dFGRS and GAMA (2 mag deeper). We stress again here that our first data point might be affected by the apparent richness selection we applied on the group catalogue. If we exclude this data point, the agreement with Eke et al. (2004) is fairly reasonable.

We also compare our results with a lensing analysis of MaxBCG clusters (Koester et al. 2007) using SDSS imaging (Sheldon et al. 2009). We show their result as the green points in Fig. 13. In this case the groups/clusters were binned according to their total luminosity and the masses were measured by first inverting the ESD signal to 3D density and mass profiles and then by inferring the mass inside R_{200}. Also in this case we find a reasonable agreement once we exclude our first data point, which, as discussed, might be affected by the apparent richness selection we applied to the group catalogue.

Finally Parker et al. (2005) considered a sample of 116 groups from the CNOC2 survey (Yee et al. 1998). The halo masses were measured by fitting an SIS profile to the stacked ESD signal measured using weak gravitational lensing. In this case, the luminosity was measured in B band. Given the small sample of groups, only two measurements were possible at quite low group luminosity. We show their results as the magenta points in Fig. 13. Following Jee et al. (2014), we applied a 0.8 multiplicative correction to the B-band mass-to-light ratio in order to have an estimate for the mass-to-light ratio in r band.

Only the mass-to-light ratio measurement in the high-luminosity bin of the CNOC2 analysis, which corresponds to our low-luminosity bin, can be directly compared to our analysis, given the luminosity range we probe. We find good agreement.

6.2 The relation between halo mass and velocity dispersion

Next, we focus on the scaling relation between the total halo mass and the group velocity dispersion. Again, we bin the groups in six bins according to their velocity dispersion, with the boundaries chosen so that the signal-to-noise ratios of the stacked ESD profiles are equal (see Table 2). The halo masses in each bin are then found by a joint halo model fit to the ESD profile in each velocity dispersion bin. Fig. 14 shows the corresponding results. The GAMA groups span an order of magnitude in velocity dispersion, but most of the
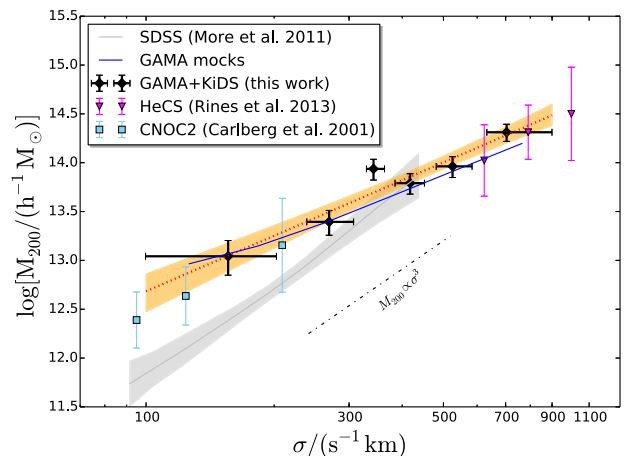

Figure 14. Halo mass as a function of the group velocity dispersion. The black points show the halo masses derived in this work from a halo model fit to the stacked ESD profile of groups with at least five members brighter than the GAMA magnitude limits. The red line shows the best-fitting power-law to the data points and the orange area indicates our estimate of the 1σ dispersion around this relation. The cyan points show the results from the CNOC2 survey (Carlberg et al. 2001), while the magenta points show the results from the HeCS sample of clusters (Rines et al. 2013). The grey band shows the mass–velocity dispersion relation obtained from measurements of satellite kinematics in SDSS (More et al. 2011). Finally, the blue line shows the relation calculated from the GAMA mocks using the same selection function applied to the data.

constraining power for the scaling relation comes from groups with $\sigma \sim 500 \, \text{km}\,\text{s}^{-1}$. This is expected given that the cut imposed on group apparent richness excludes the low-mass systems from this analysis, and that the survey volume is relatively small, and hence our sample does not contain many very massive galaxy clusters. As in the case of binning by luminosity, we believe that the apparent richness cut imposed on the GAMA group catalogue will have a non-negligible effect on the measurement of the average halo mass in the first velocity dispersion bin $\sigma < 200 \, \text{km}\,\text{s}^{-1}$.

At low velocity dispersion, we compare our results with those from the CNOC2 survey (Carlberg et al. 2001), for which the mass measurements are derived from the dynamical properties of the groups. In Fig. 14, we show the average CNOC2 mass measurements in three velocity dispersion bins; the error bars are the 1σ scatter between measurements in each bin.

At high velocity dispersion, we compare our results to the analysis of the HeCS sample (Rines et al. 2013), where masses are measured using a redshift-space caustic technique. The mean redshift of the HeCS clusters is similar to that of the GAMA groups. As for the CNOC2 sample, we binned the HeCS clusters according to their velocity dispersion, and we calculated the median mass and the 1σ dispersion in each bin. Both the CNOC2 and the HeCS sample agree well with the mass–velocity dispersion relation we derived using galaxy groups from GAMA.

We fit a power law between the halo mass and the group velocity dispersion (using the same procedure outlined in the previous section) and we constrain this relation to be

$$\left(\frac{M_{200}}{10^{14} \, h^{-1} \, \text{M}_\odot}\right) = (1.00 \pm 0.15) \left(\frac{\sigma}{500 \, \text{s}^{-1}\,\text{km}}\right)^{(1.89 \pm 0.27)}. \quad (38)$$

We find that the average scatter in the halo mass–velocity dispersion relation is $\sigma_{\log\langle M_{200}\rangle} = 0.20$.

We do not see any indication of a change in the slope over almost two order of magnitude in mass, from massive clusters to small groups. However, the slope we find is significantly shallower than what would be expected from a virial scaling relation ($M \propto \sigma^3$) as is seen in dissipationless numerical simulation (Evrard et al. 2008). A very similar result ($M \propto \sigma^{2.09 \pm 0.34}$) was found by a previous weak lensing analysis of the same group catalogue using SDSS galaxies as background sources (Han et al. 2015).

There are at least two possible explanations for this effect.

(i) Hydrodynamical simulations have shown that galaxies trace shallower mass–velocity dispersion relations (slope lower than 3) than dark matter particles (Munari et al. 2013). This is due to dynamical friction and tidal disruption, acting on substructures and galaxies, but not on dark matter particles. The typical effect measured in simulations is of the order of 10 per cent, which is too small to explain the value of the power-law slope we measure when comparing with the virial expectation.

(ii) The apparent richness cut we imposed to the group catalogue, the GAMA selection function and the limited cosmological volume we probe might introduce selection biases on our mass measurements. In particular, the apparent richness cut might introduce a positive bias for mass-measurements in the lowest velocity dispersion bin, and the small volume used in this work might introduce negative biases in the highest velocity dispersion bins. The combination of these two effects would result in a shallower mass–velocity dispersion relation.

To investigate the second hypothesis further, we compare our inferred scaling relation with one measured from the dark matter only

mock GAMA catalogue (R+11; Merson et al. 2013) applying the same apparent richness cut. In the GAMA mocks the velocity dispersion is measured using the underlying/true dark matter haloes while the stored mass of the haloes (DHalo mass) are computed as the sum of the masses of their component subhaloes (Jiang et al. 2014). For the purpose of the comparison we convert them into M_{200} (McNaught-Roberts, in preparation). We show the results as the blue line in Fig. 14. We find good agreement with the scaling relation measured from the data, supporting the hypothesis that the shallower scaling relation we measure is mostly caused by selection effects. However, we cannot exclude at this stage that part of the reason for the shallower mass–velocity dispersion relation might be dynamical processes acting on the galaxies in the groups.

A detailed investigation will be presented in a forthcoming paper (Robotham et al., in preparation) in the context of finding optimal dynamical mass estimates using weak lensing measurements of the group masses.

Finally, we compare our results with measurements of the mass–velocity dispersion relation obtained from measurements of satellite kinematics in SDSS (More et al. 2011). In this case, we extrapolate the mass–velocity dispersion relation from measurements of the stellar mass – halo mass and stellar mass – velocity dispersion relations which are provided in that paper. Note that these two relations have not been derived independently from each other. We find good agreement with our results for $\sigma > 300 \, \text{km}\,\text{s}^{-1}$. For lower mass haloes, we have already discussed the potential selection effect due to the apparent richness cut that affects our first data point. However, we also note that there is some tension between the CNOC2 results (Carlberg et al. 2001) and the SDSS satellite kinematics results. In general, velocity dispersion and mass measurements are more difficult for low-mass groups than for massive systems because of the smaller number of members and more severe selection effects.

6.3 The relation between halo mass and *r*-band luminosity fraction of the BCG

Feedback from supernovae (Dekel & Silk 1986) and AGNs (Springel, Di Matteo & Hernquist 2005a) have been proposed in the past decade as a possible solution for reducing the star formation efficiency in hydrodynamical simulations (e.g. Sijacki et al. 2007; Fabjan et al. 2010; McCarthy et al. 2010; Booth & Schaye 2013; Vogelsberger et al. 2014; Schaye et al. 2015 and references therein). It is important to test the hypothesis of feedback and to constrain its efficiency by comparing complementary predictions of hydrodynamical simulations with observations. Motivated by the work of Le Brun et al. (2014), we focus here on the relation between the *r*-band luminosity fraction of the BCG, defined as $L_{\text{BCG}}/L_{\text{grp}}$, and the group halo masses calculated in this work by binning the groups according to $L_{\text{BCG}}/L_{\text{grp}}$ (see Table 2). The *r*-band luminosity of the BCG is calculated from the r_{AB} petrosian magnitude from the GAMA catalogue. We apply a *k*-correction and evolution correction to the magnitude following R+11:

$$(k+e)(z) = \sum_{i=0}^{4} a_i (z - 0.2)^i - 1.75z, \quad (39)$$

with $a_i = [0.2085, 1.0226, 0.5237, 3.5902, 2.3843]$. We note that the original correction presented in equation (8) in R+11 presents an error in the sign of the last term in the above equation. Fig. 15 shows the halo masses obtained for groups stacked according to $L_{\text{BCG}}/L_{\text{grp}}$ as a function of $L_{\text{BCG}}/L_{\text{grp}}$.
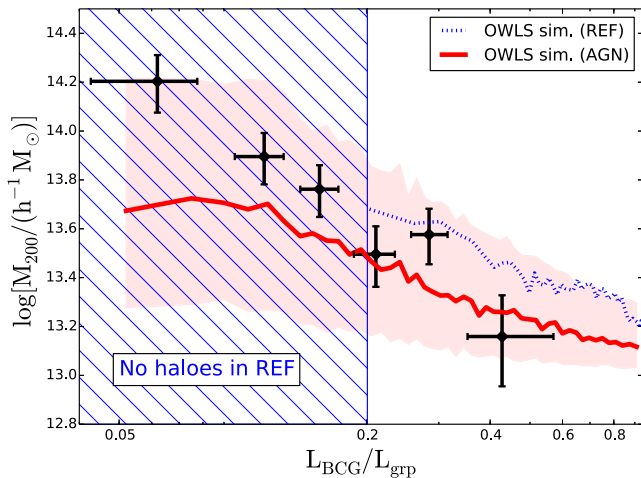
Figure 15. Group masses as a function of the *r*-band luminosity fraction of the BCG. The solid black points show the halo masses derived in this work from a halo model fit to the stacked ESD profile of groups with at least five members brighter than the GAMA magnitude limit. The solid red and the dashed blue lines are predictions from the Cosmo-OWLS simulation at the median redshift of the GAMA groups for a run including AGN feedback and a reference run without AGN feedback (Le Brun et al. 2014). The luminosities measured in the simulation are $(k + e)$ corrected to redshift 0 using the same functional form (equation 39) applied to the data. The red area encompasses the 16th and 84th percentile of the mass distribution in each luminosity fraction bin for the AGN simulation. The shaded blue area indicates the range in $L_{\rm BCG}/L_{\rm grp}$ in which there are no haloes in the REF simulation.

There is a clear trend of group masses with the *r*-band luminosity fraction of the BCG. This trend has been previously observed at group scales by Rasmussen & Ponman (2009) and at cluster scales by Lin & Mohr (2004). The explanation is that the growth of the BCG is modest compared with the growth of the entire group.

Since the luminosity of the BCG is proportional to its stellar mass content and the group luminosity is an increasing function of the total halo mass, one can compare the results reported in this paper with studies of the stellar-to-halo mass ratio (SHMR) as a function of halo mass (e.g. George et al. 2011; Leauthaud et al. 2012b; van der Burg et al. 2014; Coupon et al. 2015). There is a clear consensus on the decline of the SHMR with halo mass, which is a different manifestation of the trend displayed in Fig. 15 where we report the halo mass as a function of the *r*-band luminosity fraction of the BCG. In particular, for central galaxies, it has been shown (Behroozi et al. 2013; Coupon et al. 2015) that haloes of $\sim 2 \times 10^{14}\, h^{-1}\, {\rm M_\odot}$ have an SHMR about an order of magnitude lower than that of haloes of $\sim 10^{13}\, h^{-1}\, {\rm M_\odot}$, again in qualitative agreement with the result shown in Fig. 15. The steep decline of the relation between the group mass and the *r*-band luminosity fraction is a consequence of star formation becoming less efficient in more massive haloes. Several mechanisms, beyond AGN feedback, have been invoked to explain this phenomenon such as halo mass quenching (e.g. Peng et al. 2010; Ilbert et al. 2013) or the presence of many satellite galaxies in massive haloes which cut off the gas supply to the BCG (Aragon-Calvo, Neyrinck & Silk 2014).

We focus here in particular on comparing our results with the (Cosmo-) OverWhelmingly Large Simulations (OWLS; Schaye et al. 2010; Le Brun et al. 2014).

Le Brun et al. (2014) present results from these simulations in terms of *K*-band luminosity binned by halo mass. They report a very similar trend to the one we observe in our data. In particular,

they find a large difference in the luminosity fraction of the BCG when they compare simulations with and without AGN feedback. To compare our results with the Cosmo-OWLS simulation, the *r*-band results were provided by the Cosmo-OWLS team using the same *K*-correction and evolution correction we applied to the data (equation 39) for three redshifts snapshots $z = [0.125, 0.25, 0.375]$. When comparing the simulations to the data, we use the results from the snapshots closer to the median redshift of the GAMA groups. We discarded from the simulation all haloes with mass lower than $10^{13}\, h^{-1}\, {\rm M_\odot}$, which roughly corresponds to the minimum mass of groups with more than five members in the G^{3}Cv7 catalogue (see Section 6.4). In this way, we try to mimic the selection we applied to the data. Finally, we bin the simulation in the same way we bin the data, using the BCG luminosity fraction as a proxy for the group mass.

Fig. 15 shows the Cosmo-OWLS results for the run including AGN feedback (solid red line) and for a reference run (REF) without AGN (dashed blue lines). The red area encompasses the 16th and 84th percentile of the mass distribution in each luminosity fraction bin.

For $L_{\rm BCG}/L_{\rm grp} < 0.2$ the reference run does not contain any groups which on the contrary are clearly present in our group sample. The reason for this is that the gas cooling in the REF simulation is too efficient, leading to BCGs which are always very luminous in comparison to the total luminosity of the group. This evidence alone is sufficient to conclude that the data disfavour a model without AGN feedback. Note that this conclusion is independent of the group mass measurements. Our derived scaling relation between the halo mass and the luminosity fraction of the BCG for $L_{\rm BCG}/L_{\rm grp} > 0.2$ further supports the above conclusion, being in reasonable agreement with the prediction from the simulation including AGN feedback. A detailed comparison of the trend in Fig. 15 with simulations would require replicating the GAMA group finder and selection function on the Cosmo-OWLS simulations and is beyond the scope of this paper.

6.4 The relation between halo mass and group apparent richness

Finally, we investigate the relation between the total halo mass and the apparent richness of the groups. The groups are binned according to their apparent richness (see Table 2), and the average halo mass for each bin is estimated by fitting a halo model to the stacked ESD profile. We show the result in Fig. 16.

We parametrize the halo mass–richness relation with a power law, which is fitted to the data with the same procedure outlined in the previous sections:

$$\left(\frac{M_{200}}{10^{14}\, h^{-1}\, {\rm M_\odot}} \right) = (0.43 \pm 0.08) \left(\frac{N_{\rm fof}}{10} \right)^{(1.09 \pm 0.18)}, \qquad (40)$$

and we constrain the average scatter in the halo mass–richness relation to be $\sigma_{\log\langle M_{200}\rangle} = 0.20$.

As expected, richer groups are also more massive. We caution the reader that this scaling relation is the one most affected by the GAMA selection function. In fact, unlike our treatment of the total group luminosity, we do not correct the apparent richness measurements to account for the faint galaxy members not targeted by GAMA. We compare our results with the GAMA mocks, which have the same selection function as the data, and we generally find good agreement.
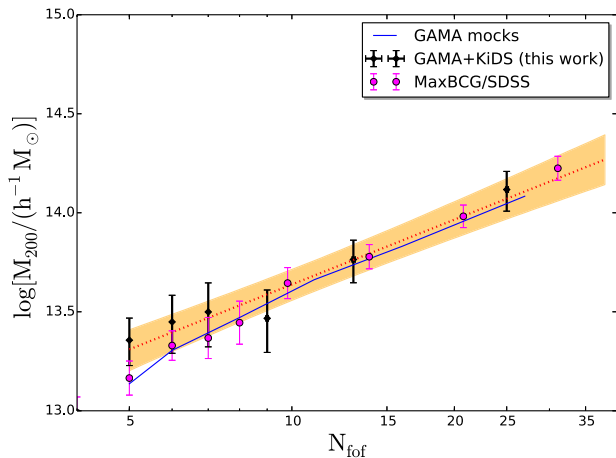
Figure 16. Group halo mass as a function of the richness (N_{fof}). We use here only groups with at least five members brighter than $r_{AB} = 19.8$. The richness of the groups is not corrected to account for the fainter galaxies not targeted by GAMA. The red line shows the best-fitting power-law relation to the data points. Our estimate of the 1σ dispersion around this relation is shown as the orange area. The blue line shows the mass–richness relation derived from the GAMA mocks using the same selection function applied to the data. The magenta points show the result of a weak lensing analysis of 130 000 groups and clusters of galaxies in the SDSS (Johnston et al. 2007).

We also compare our results with a weak lensing analysis of 130 000 groups and clusters of galaxies in the SDSS (Johnston et al. 2007). The masses were derived from fitting an halo model to the stacked ESD profile in 12 richness bins. The richness was defined as the number of red sequence galaxies with luminosities larger than $0.4L_\star$ within a given projected radius, which is close to R_{200}. In spite of the different richness definitions we find good agreement with our measurements, both for the amplitude and the slope of the mass–richness relation.

7 CONCLUSIONS

In this paper, we present the first weak lensing analysis of the mass distribution in the GAMA groups using background sources from the overlapping KiDS survey. The effective overlapping area (accounting for masks) used in this work is 68.5 deg² and corresponds to the first two data releases of *ugri* images of the KiDS data (de Jong et al. 2015 and K+15).

Our main results are the following.

(i) We measure the stacked ESD profile of the galaxy groups as a function of their total *r*-band luminosity, velocity dispersion, fraction of group light in the BCG and apparent richness. Splitting the data into six roughly equal signal-to-noise bins, we derive average halo masses per bin with a typical precision of 0.12 dex. We provide a physical interpretation of the signal using the halo model.

(ii) We show the importance of modelling the mis-centring of the BCG (used here as tracer of the group centre) with respect to the centre of the group's dark matter halo in order to derive unbiased results, in particular on the halo mass–concentration relation.

(iii) Our results are consistent with the normalization of the halo mass–concentration relation proposed by Duffy et al. (2008), when mis-centring is included in the model.

(iv) We find no evidence of a significant baryonic component in the centre of the groups in excess of the stellar mass of the BCG. However, the uncertainty on this result is quite large due to

the low signal-to-noise at small scales, which is in turn caused by the difficulties inherent in measuring reliable shapes for blended objects.

(v) We obtain clear scaling relations between the halo mass and a number of observable properties of the groups: the group *r*-band luminosity, the velocity dispersion of the group, its apparent richness and the ratio between the *r*-band luminosity of the BCG and the total *r*-band luminosity of the group. The typical scatter in halo mass at fixed observable property is $\sigma_{\log\langle M_{200}\rangle} = 0.2$.

(vi) We show that our data have the statistical power to discriminate between models with and without AGN feedback and possibly between different AGN feedback models.

This analysis is part of the first set of weak lensing results using the KiDS data, based on data obtained during the first two years of operation. As the survey continues to cover more sky, both the statistical power and the fidelity of the measurements will grow, further refining these results as well as enabling other analyses of the distribution of dark matter in galaxies, groups, and clusters.

STFC (UK), the ARC (Australia), the AAO, and the participating institutions. The GAMA website is http://www.gama-survey.org/.

Author Contributions: All authors contributed to the development and writing of this paper. The authorship list reflects the lead authors (MV, MC, MB, KK) followed by two alphabetical groups. The first alphabetical group includes those who are key contributors to both the scientific analysis and the data products. The second group covers those who have either made a significant contribution to the data products, or to the scientific analysis.

REFERENCES

Aragon-Calvo M. A., Neyrinck M. C., Silk J., 2014, preprint (arXiv:e-prints)
Baldry I. K. et al., 2010, MNRAS, 404, 86
Baldry I. K. et al., 2014, MNRAS, 441, 2440
Bartelmann M., Schneider P., 2001, Phys. Rep., 340, 291
Behroozi P. S., Conroy C., Wechsler R. H., 2010, ApJ, 717, 379
Behroozi P. S., Wechsler R. H., Conroy C., 2013, ApJ, 762, L31
Benítez N., 2000, ApJ, 536, 571
Berlind A. A. et al., 2006, ApJS, 167, 1
Booth C. M., Schaye J., 2013, Sci. Rep., 1738
Bower R. G., Benson A. J., Malbon R., Helly J. C., Frenk C. S., Baugh C. M., Cole S., Lacey C. G., 2006, MNRAS, 370, 645
Brainerd T. G., Blandford R. D., Smail I., 1996, ApJ, 466, 623
Brough S., Forbes D. A., Kilborn V. A., Couch W., 2006, MNRAS, 370, 1223
Bruzual G., Charlot S., 2003, MNRAS, 344, 1000
Bullock J. S., Kolatt T. S., Sigad Y., Somerville R. S., Kravtsov A. V., Klypin A. A., Primack J. R., Dekel A., 2001, MNRAS, 321, 559
Cacciato M., van den Bosch F. C., More S., Li R., Mo H. J., Yang X., 2009, MNRAS, 394, 929
Cacciato M., van den Bosch F. C., More S., Mo H., Yang X., 2013, MNRAS, 430, 767
Calzetti D., Armus L., Bohlin R. C., Kinney A. L., Koornneef J., Storchi-Bergmann T., 2000, ApJ, 533, 682
Capaccioli M., Schipani P., 2011, The Messenger, 146, 2
Carlberg R. G., Yee H. K. C., Morris S. L., Lin H., Hall P. B., Patton D. R., Sawicki M., Shepherd C. W., 2001, ApJ, 552, 427
Chabrier G., 2003, ApJ, 586, L133
Chang C. et al., 2013, MNRAS, 434, 2121
Choi A., Tyson J. A., Morrison C. B., Jee M. J., Schmidt S. J., Margoniner V. E., Wittman D. M., 2012, ApJ, 759, 101
Colless M. et al., 2001, MNRAS, 328, 1039
Cooray A., Sheth R., 2002, Phys. Rep., 372, 1
Coupon J. et al., 2015, MNRAS, 449, 1352
de Jong J. T. A., Verdoes Kleijn G. A., Kuijken K. H., Valentijn E. A., 2013, Exp. Astron., 35, 25
de Jong J. T. A. et al., 2015, preprint (arXiv:1507.00742)
Dekel A., Silk J., 1986, ApJ, 303, 39
Driver S. P. et al., 2011, MNRAS, 413, 971
Dubois Y., Gavazzi R., Peirani S., Silk J., 2013, MNRAS, 433, 3297
Duffy A. R., Schaye J., Kay S. T., Dalla Vecchia C., 2008, MNRAS, 390, L64
Dutton A. A., Macciò A. V., 2014, MNRAS, 441, 3359
Eckmiller H. J., Hudson D. S., Reiprich T. H., 2011, A&A, 535, A105
Eke V. R., Navarro J. F., Steinmetz M., 2001, ApJ, 554, 114
Eke V. R. et al., 2004, MNRAS, 355, 769
Erben T. et al., 2013, MNRAS, 433, 2545
Evrard A. E. et al., 2008, ApJ, 672, 122
Fabjan D., Borgani S., Tornatore L., Saro A., Murante G., Dolag K., 2010, MNRAS, 401, 1670
Fedeli C., 2014, JCAP, 4, 28
Finoguenov A. et al., 2015, A&A, 576, A130
Fischer P. et al., 2000, AJ, 120, 1198
Gelman A., Rubin D. B., 1992, Stat. Sci., 7, 457
George M. R. et al., 2011, ApJ, 742, 125
George M. R. et al., 2012, ApJ, 757, 2
Gerke B. F. et al., 2005, ApJ, 625, 6
Giocoli C., Meneghetti M., Ettori S., Moscardini L., 2012, MNRAS, 426, 1558
Han J. et al., 2015, MNRAS, 446, 1356
Heymans C. et al., 2006, MNRAS, 371, L60
Hildebrandt H. et al., 2012, MNRAS, 421, 2355
Hoekstra H., 2004, MNRAS, 347, 1337
Hoekstra H. et al., 2001, ApJ, 548, L5
Hudson M. J. et al., 2015, MNRAS, 447, 298
Ilbert O. et al., 2013, A&A, 556, A55
Jee M. J., Hoekstra H., Mahdavi A., Babul A., 2014, ApJ, 783, 78
Jiang L., Helly J. C., Cole S., Frenk C. S., 2014, MNRAS, 440, 2115
Johnston D. E., Sheldon E. S., Tasitsiomi A., Frieman J. A., Wechsler R. H., McKay T. A., 2007, ApJ, 656, 27
Kettula K. et al., 2013, ApJ, 778, 74
Kitching T. D., Miller L., Heymans C. E., van Waerbeke L., Heavens A. F., 2008, MNRAS, 390, 149
Klypin A. A., Trujillo-Gomez S., Primack J., 2011, ApJ, 740, 102
Knobel C. et al., 2009, ApJ, 697, 1842
Kobayashi M. I. N., Leauthaud A., More S., Okabe N., Laigle C., Rhodes J., Takeuchi T. T., 2015, MNRAS, 449, 2128
Koester B. P. et al., 2007, ApJ, 660, 239
Kuijken K., 2008, A&A, 482, 1053
Kuijken K., 2011, The Messenger, 146, 8
Kuijken K. et al., 2015, preprint (arXiv:1507.00738) (K+15)
Le Brun A. M. C., McCarthy I. G., Schaye J., Ponman T. J., 2014, MNRAS, 441, 1270
Leauthaud A. et al., 2010, ApJ, 709, 97
Leauthaud A. et al., 2012a, ApJ, 744, 159
Leauthaud A. et al., 2012b, ApJ, 746, 95
Lin Y.-T., Mohr J. J., 2004, ApJ, 617, 879
Liske J. et al., 2005, MNRAS, in press
Loveday J. et al., 2012, MNRAS, 420, 1239
Loveday J. et al., 2015, MNRAS, 451, 1540
McCarthy I. G. et al., 2010, MNRAS, 406, 822
Macciò A. V., Dutton A. A., van den Bosch F. C., 2008, MNRAS, 391, 1940
McFarland J. P., Verdoes-Kleijn G., Sikkema G., Helmich E. M., Boxhoorn D. R., Valentijn E. A., 2013, Exp. Astron., 35, 45
McNaught-Roberts T. et al., 2014, MNRAS, 445, 2125
Mahdavi A., Hoekstra H., Babul A., Bildfell C., Jeltema T., Henry J. P., 2013, ApJ, 767, 116
Mandelbaum R., Seljak U., Cool R. J., Blanton M., Hirata C. M., Brinkmann J., 2006, MNRAS, 372, 758
Mandelbaum R., Seljak U., Hirata C. M., 2008, JCAP, 8, 6
Melchior P., Viola M., 2012, MNRAS, 424, 2757
Merson A. I. et al., 2013, MNRAS, 429, 556
Miller L., Kitching T. D., Heymans C., Heavens A. F., van Waerbeke L., 2007, MNRAS, 382, 315
Miller L., Heymans C., Kitching T. D., van Waerbeke L., Erben T., Hildebrandt H., 2013, MNRAS, 429, 2858
Miyatake H. et al., 2015, ApJ, 806, 1
More S., van den Bosch F. C., Cacciato M., Mo H. J., Yang X., Li R., 2009a, MNRAS, 392, 801
More S., van den Bosch F. C., Cacciato M., 2009b, MNRAS, 392, 917
More S., van den Bosch F. C., Cacciato M., Skibba R., Mo H. J., Yang X., 2011, MNRAS, 410, 210
More S., Miyatake H., Mandelbaum R., Takada M., Spergel D. N., Brownstein J. R., Schneider D. P., 2015, ApJ, 806, 2
Moster B. P., Somerville R. S., Maulbetsch C., van den Bosch F. C., Macciò A. V., Naab T., Oser L., 2010, ApJ, 710, 903
Moster B. P., Naab T., White S. D. M., 2013, MNRAS, 428, 3121
Munari E., Biviano A., Borgani S., Murante G., Fabjan D., 2013, MNRAS, 430, 2638
Murray S. G., Power C., Robotham A. S. G., 2013, MNRAS, 434, L61
Nagai D., Vikhlinin A., Kravtsov A. V., 2007, ApJ, 655, 98
Navarro J. F., Frenk C. S., White S. D. M., 1995, MNRAS, 275, 720 (NFW)
Norberg P., Baugh C. M., Gaztañaga E., Croton D. J., 2009, MNRAS, 396, 19

Oguri M., Takada M., 2011, Phys. Rev. D, 83, 023008
Parker L. C., Hudson M. J., Carlberg R. G., Hoekstra H., 2005, ApJ, 634, 806
Pearson R. J., Ponman T. J., Norberg P., Robotham A. S. G., Farr W. M., 2015, MNRAS, 449, 3082
Peng Y.-j. et al., 2010, ApJ, 721, 193
Planck Collaboration XVI, et al., 2014, A&A, 571, A16
Prada F., Klypin A. A., Cuesta A. J., Betancort-Rijo J. E., Primack J., 2012, MNRAS, 423, 3018
Rasia E. et al., 2006, MNRAS, 369, 2013
Rasmussen J., Ponman T. J., 2009, MNRAS, 399, 239
Refregier A., Kacprzak T., Amara A., Bridle S., Rowe B., 2012, MNRAS, 425, 1951
Rines K., Geller M. J., Diaferio A., Kurtz M. J., 2013, ApJ, 767, 15
Robotham A. et al., 2010, PASA, 27, 76
Robotham A. S. G. et al., 2011, MNRAS, 416, 2640 (R+11)
Robotham A. S. G. et al., 2013, MNRAS, 431, 167
Sales L. V., Navarro J. F., Schaye J., Dalla Vecchia C., Springel V., Booth C. M., 2010, MNRAS, 409, 1541
Schaye J. et al., 2010, MNRAS, 402, 1536
Schaye J. et al., 2015, MNRAS, 446, 521
Seljak U., 2000, MNRAS, 318, 203
Semboloni E., Hoekstra H., Schaye J., van Daalen M. P., McCarthy I. G., 2011, MNRAS, 417, 2020
Semboloni E., Hoekstra H., Schaye J., 2013, MNRAS, 434, 148
Shan H. et al., 2015, preprint (arXiv:1502.00313)
Sheldon E. S. et al., 2004, AJ, 127, 2544
Sheldon E. S. et al., 2009, ApJ, 703, 2232
Sheth R. K., Tormen G., 1999, MNRAS, 308, 119
Sheth R. K., Mo H. J., Tormen G., 2001, MNRAS, 323, 1
Sifón C. et al., 2015, preprint (arXiv:1507.00737)
Sijacki D., Springel V., Di Matteo T., Hernquist L., 2007, MNRAS, 380, 877
Skibba R. A., Macciò A. V., 2011, MNRAS, 416, 2388
Spergel D. N., Flauger R., Hložek R., 2015, Phys. Rev. D, 91, 023518
Springel V., Di Matteo T., Hernquist L., 2005a, MNRAS, 361, 776
Springel V. et al., 2005b, Nature, 435, 629
Sun M., Voit G. M., Donahue M., Jones C., Forman W., Vikhlinin A., 2009, ApJ, 693, 1142
Taylor E. N. et al., 2011, MNRAS, 418, 1587
Tinker J., Kravtsov A. V., Klypin A., Abazajian K., Warren M., Yepes G., Gottlöber S., Holz D. E., 2008, ApJ, 688, 709
Tinker J. L., Robertson B. E., Kravtsov A. V., Klypin A., Warren M. S., Yepes G., Gottlöber S., 2010, ApJ, 724, 878
Vale A., Ostriker J. P., 2004, MNRAS, 353, 189
van Daalen M. P., Schaye J., Booth C. M., Dalla Vecchia C., 2011, MNRAS, 415, 3649
van den Bosch F. C. et al., 2007, MNRAS, 376, 841
van den Bosch F. C., More S., Cacciato M., Mo H., Yang X., 2013, MNRAS, 430, 725
van der Burg R. F. J., Muzzin A., Hoekstra H., Wilson G., Lidman C., Yee H. K. C., 2014, A&A, 561, A79
van Uitert E., Hoekstra H., Velander M., Gilbank D. G., Gladders M. D., Yee H. K. C., 2011, A&A, 534, A14
van Uitert E., Cacciato M., Hoekstra H., Herbonnet R., 2015, A&A, 579, A26
Velander M. et al., 2014, MNRAS, 437, 2111
Viola M., Kitching T. D., Joachimi B., 2014, MNRAS, 439, 1909
Vogelsberger M. et al., 2014, Nature, 509, 177
Wetzel A. R., Tinker J. L., Conroy C., Bosch F. C. v. d., 2014, MNRAS, 439, 2687
Yang X., Mo H. J., van den Bosch F. C., 2009, ApJ, 695, 900
Yee H. K. C. et al., 1998, Highlights Astron., 11, 460

APPENDIX A: ALTERNATIVE DEFINITIONS OF THE GROUP CENTRE

We present here the measurements of the stacked ESD profile and the halo model constraints we obtain if we use a different definition of the group centre, compared to the BCG definitions used throughout the paper.

In Fig. A1, we show the stacked ESD profile for the same six luminosity bins used in Section 5 but now using the brightest galaxy left after iteratively removing the most distant galaxies from the group centre of light which is labelled as `IterCen` (left-hand panel) and the group centre of light `Cen` (right-hand panel) as the definition for the group centre. When `IterCen` is used, the stacked signal is statistically indistinguishable from the case when `BCG` is used as the group centre. This is not surprising since the two centre definitions differ only for a few per cent of the groups.

When `Cen` is used as the group centre, the shape of the stacked ESD profile is very different. The turnover of the signal at scales around 100 h^{-1} kpc is a clear indication of mis-centring between the chosen centre of the halo group and the true minimum of the halo potential well. R+11 report that `Cen` is not a good proxy for the halo centre, and hence, this result is not surprising. It is clear in this case that not including the mis-centring parameters in the model would lead to a very poor description of the data. We do not show the posterior distributions for the halo model parameters corresponding to the case of `Cen`. The degeneracies between the parameters are the same as those found when `BCG` or `IterCen` are used as proxies for the halo centre. We can derive tight constraints on the probability of mis-centring $p_{\rm off} \geq 0.67 \, 2\sigma$, and we find that on average the amount of offset of the centre of light with respect to the minimum of the halo potential well is $\mathcal{R}_{\rm off} = 1.00^{+0.37}_{-0.51}$. We summarize the results in Tables 3 and 4.

The constraints we derive for the halo masses in the six luminosity bins and the constraints on $\sigma_{\log \bar{M}}, f_c, A_{\rm P}$ are consistent within 1σ with the constraints derived using the other two definitions of the halo centre. These results highlight the importance of a proper model of the mis-centring in the analysis of the lensing signal from groups or clusters of galaxies. Neglecting mis-centring could lead to biases in the derived masses and in the other model parameters, particularly the halo concentration.
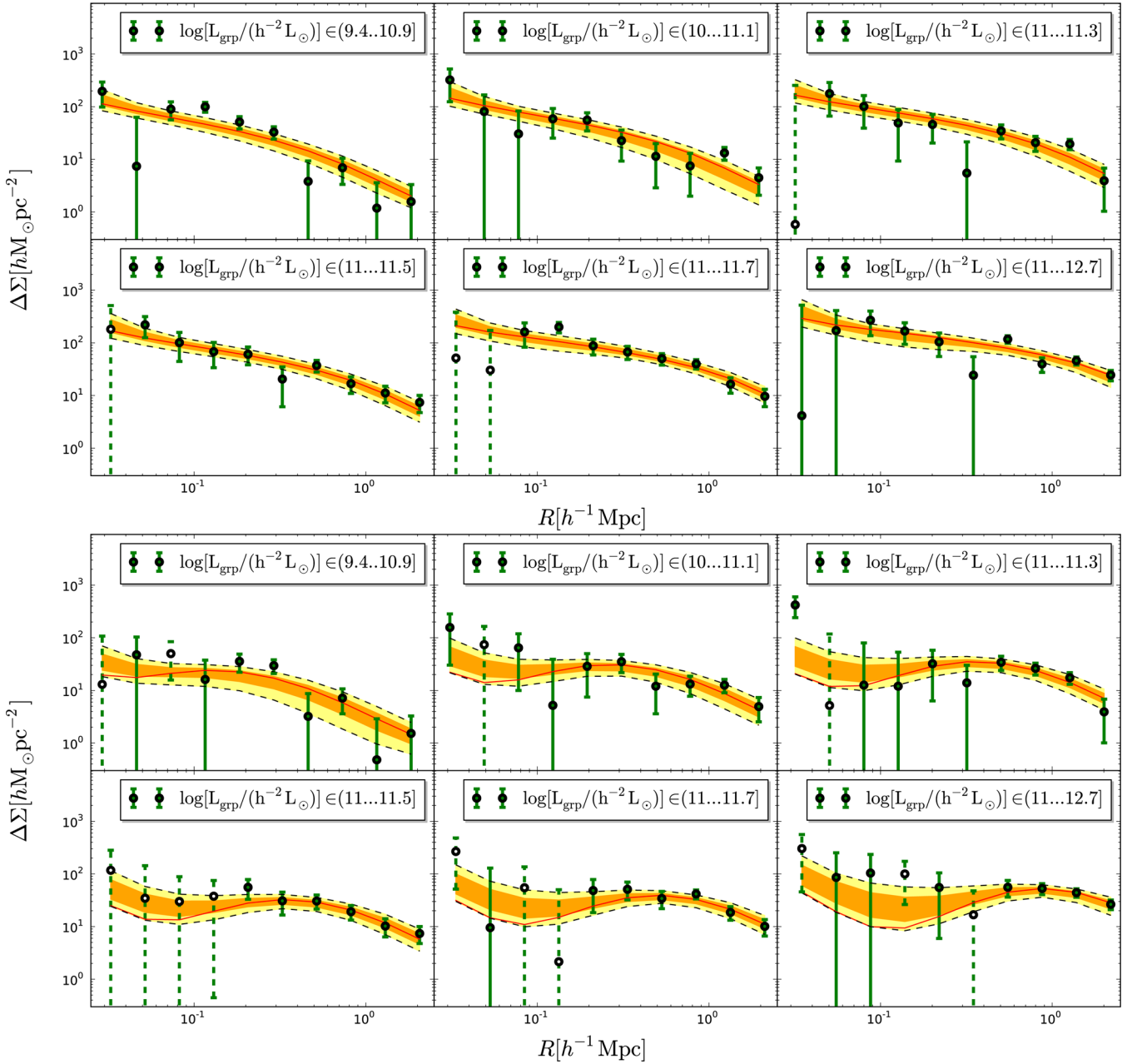
Figure A1. Stacked ESD measured around the groups' IterCen (upper panel) and the groups' centre of light Cen (lower panel) for six group luminosity bins as a function of distance from the group centre. The group luminosity increases from left to right and from top to bottom. The stacking of the signal has been performed considering only groups with $N_{\rm fof} \geq 5$. The error bars on the stacked signal are computed as detailed in Section 3.4. The orange and yellow bands represent the 68 and 95 percentile of the model around the median and the red lines indicate the best-fitting model.

This paper has been typeset from a TeX/LaTeX file prepared by the author.